Chemical Engineering Journal 513 (2025) 163072

Contents lists available at ScienceDirect

Chemical Engineering Journal

journal homepage: www.elsevier.com/locate/cej

Urea synthesis by Plasmon-Assisted N_2 and CO_2 co-electrolysis onto heterojunctions decorated with silver nanoparticles

Leandro A. Faustino [a,*], Leonardo D. de Angelis [a], Eduardo C. de Melo [a], Giliandro Farias [b], Egon C. dos Santos [b], Caetano R. Miranda [b], Ana G. Buzanich [c], Roberto M. Torresi [a], Paulo F.M. de Oliveira [a], Susana I. Córdoba de Torresi [a,*]

[a] Instituto de Química, Universidade de São Paulo, Av. Prof. Lineu Prestes 748, 05508-900, São Paulo, SP, Brazil
[b] Instituto de Física, Universidade de São Paulo, R. do Matão 1371, 05508-090, São Paulo, SP, Brazil
[c] Federal Institute of Materials Research and Testing (BAM), Richard-Willstaetter-Str. 12, 12489 Berlin, Germany

ARTICLE INFO

Keywords:
Silver nanoparticles
Bismuth nanoparticles
Plasmonic catalysis
C-N coupling
N_2 reduction reaction
CO_2 reduction reaction

ABSTRACT

The $N_2 + CO_2$ co-electrolysis to urea synthesis has become a promising alternative to the energy intensive traditional processes for urea production. However, there are still challenges in this approach, especially due to the competition with HER (Hydrogen Evolution Reaction) leading to low efficiency. Electrochemistry assisted by localized surface plasmon resonance (LSPR) using metal nanoparticles has been reported to enhance different electrochemical reactions. Here we report an electrochemical LSPR assisted urea synthesis using Ag nanoparticles (NPs) supported on $BiVO_4/BiFeO_3$ catalyst mechanochemically synthesized. The electrochemical experiments were performed under dark and upon plasmon excitation at the LSPR region of Ag NPs. Our results demonstrated that exciting in the LSPR range, urea yield rate and Faradic efficiency were considerably improved with reduced overpotential, 19.2 μmol h^{-1} g^{-1} and FE 24.4% at +0.1 V *vs* RHE compared to 9.6 μmol h^{-1} g^{-1} and FE 9.4% at −0.2 V *vs* RHE under dark conditions. Further *in situ* FTIR-RAS experiments for mechanism investigation revealed the presence of N-H and C-N intermediates and the real effect of Ag plasmon excitation on HER and $N_2 + CO_2$ co-electrolysis. Theoretical calculations confirm the energy of the species involved in C-N coupling as well the role of the complex catalytic sites, which agrees with XAS measurements.

1. Introduction

Urea is an important chemical feedstock used over several areas, especially in the fertilizer industry [1,2]. Its production process occurs through the Bosch-Meiser process, in which catalysts are employed under harsh conditions of temperature and pressure [3,4]. Although this process has been extensively employed, the associated drawbacks make it highly costly in terms of energy and a non-environmentally friendly route. From this viewpoint, new creative and innovative solutions are necessary to replace, at least partially, the traditional synthesis conditions. Mimicking the Bosch-Meiser process through electrochemistry has attracted attention. Most of the approaches consist of electrochemical activation of species such as NO, NO_2^-, NO_3^- and N_2 in the presence of CO_2 [5–10]. Gaseous N_2 is probably the most interesting candidate for nitrogen source, as the atmosphere is composed by 78% of N_2 [11]. Moreover, the use of CO_2 gas makes it even more attractive, due to its negative effect on climate change and the unfortunate exponential increase in its emissions. Thus, the use of abundant N_2 and CO_2 gases in the electrochemical urea synthesis seems the ideal scenario but several challenges are associated to it. The first one, is related to the high stability of the N≡N triple bond of N_2 and its low solubility in aqueous electrolytes [12]. Often, the experiments are carried out in aqueous electrolytes, which can result in a loss of selectivity since side reactions such as hydrogen evolution reaction (HER) can occur, competing with N_2 and CO_2 reduction [13,14]. Another fact that ensures the challenges, is the adsorption of gases over the catalyst surface [15]. Thus, to promote the C-N coupling starting from N_2 and CO_2 molecules, the catalyst must have active sites capable of adsorbing both species at the same time and close enough to interact. Different approaches have been studied related to the architecture of catalysts that includes defects in the catalyst's structure such as oxygen vacancies [16,17], frustrated Lewis pairs [18], materials based on heterojunctions [19] and the decoration

* Corresponding authors at: Instituto de Química, Universidade de São Paulo, Av. Prof. Lineu Prestes 748, 05508-900, São Paulo, SP, Brazil (L.A. Faustino).
E-mail addresses: leandrofaustino@usp.br (L.A. Faustino), storresi@iq.usp.br (S.I. Córdoba de Torresi).

https://doi.org/10.1016/j.cej.2025.163072
Received 23 January 2025; Received in revised form 16 April 2025; Accepted 24 April 2025
Available online 25 April 2025
1385-8947/

of materials with alloys and nanoparticles (NPs) [20,21]. Besides the large surface area of metal NPs, the advantage of their use also includes an improvement of the conductivity. Consequently, there is an enhancement in the catalytic and the physicochemical responses of the NPs, arising from the localized surface plasmon resonance (LSPR) upon light irradiation.

The LSPR is observed when metal NPs are light irradiated with an appropriate wavelength, in which the electromagnetic field of light induces the electron oscillation of these NPs generating dipoles. To compensate such effect, the NPs tend to restore the electromagnetic field to balance the charge over the surface. As result of these events, when both resonate, local effects can be observed, such as, increasement of near field and local temperature, and the generation of hot electrons [22].

The electrocatalysis enhanced by LSPR have gained attention for a series of relevant reactions, which includes eCO_2RR, N_2 reduction to NH_3, Hydrogen Evolution Reaction (HER) and other reactions such as ethanol oxidation and water splitting [22–28].

As before mentioned, the possibility of synthesis of urea at mild conditions has attracted attention. The electrochemical synthesis of urea is one promising approach since can be done using catalysts which operate at mild conditions. Then, the electrochemical C-N coupling enhanced by LSPR is an interesting approach. As $BiVO_4/BiFeO_3$ heterojunctions have already been proved to be catalyst for $N_2 + CO_2$ co-electrolysis to yield urea [19], in this work we describe a decoration of the $BiVO_4/BiFeO_3$ pristine heterojunction with bismuth and silver NPs by mechanochemistry giving Ag@$BiVO_4/BiFeO_3$. The Ag@$BiVO_4/BiFeO_3$ was fully characterized by different techniques of state-of-art, and then applied as catalyst for $N_2 + CO_2$ electrochemical reduction assisted by LSPR. Insights about the C-N coupling enhanced by a truly LSPR were obtained and a possible mechanism proposed.

2. Materials and methods

Experimental details such as chemicals, reagents, catalyst synthesis, characterization, experimental procedures, analysis methods and theoretical calculations can be found in Supporting Information (SI).

3. Results and discussion

3.1. Materials characterization

The structure of the pristine and mechanochemically prepared materials were characterized and Fig. 1**a** shows the PXRD patterns for the pristine $BiVO_4/BiFeO_3$. The peaks observed for the $BiVO_4/BiFeO_3$ match the XRD patterns of $BiVO_4$ and $BiFeO_3$ individually (JCPDS 98–010-0602 and 98–015-4394). In addition, small reflections at $2\theta = 23.5^\circ$ and 37° indicate the formation of a vanadium iron oxide in a non-stoichiometric ratio $Bi_{3.9}Fe_{0.41}O_{10.55}V_{1.59}$ (JCPDS 98–016-9091). On the other hand, for Ag@$BiVO_4/BiFeO_3$ prepared mechanochemically by the chemical reduction of $AgNO_3$ by $NaBH_4$ over $BiVO_4/BiFeO_3$, the resulting material is rather complex. The final Ag load in the Ag@$BiVO_4/BiFeO_3$ achieved was 5 % (m/m) determined by atomic absorption spectroscopy (AAS), which is consistent with the expected value for the synthesis. It is possible to observe that for the Ag@$BiVO_4/BiFeO_3$, the relative PXRD reflections of $BiVO_4/BiFeO_3$ are still maintained, but the signal intensity is decreased probably due to the loss of crystallinity during the milling process. Moreover, a new reflection observed at $2\theta = 27.2^\circ$ (012) matches with rhombohedral phase of metallic bismuth (JCPDS 98–006-4704), which is probably a result from the partial reduction of Bi oxides by $NaBH_4$ along with metallic Ag formation. Additional reflections at $2\theta = 38.1^\circ$ and 64.6° can be attributed either to metallic bismuth or fcc silver nanostructures (JCPDS 98–018-1730), but, since the signals for the two metal phases overlap in this range, one cannot distinguish metallic Ag and metallic Bi. To confirm the formation of metallic Bi under mechanochemical conditions, $BiVO_4/BiFeO_3$ was milled with the reducing agent, but in absence of $AgNO_3$. The PXRD pattern of this material, M−$BiVO_4/BiFeO_3$, also displays the same Bragg reflections of the Ag@$BiVO_4/BiFeO_3$ (Fig. 1**a, red**), highlighting the reflection at $2\theta = 27.2^\circ$ (012), confirming the

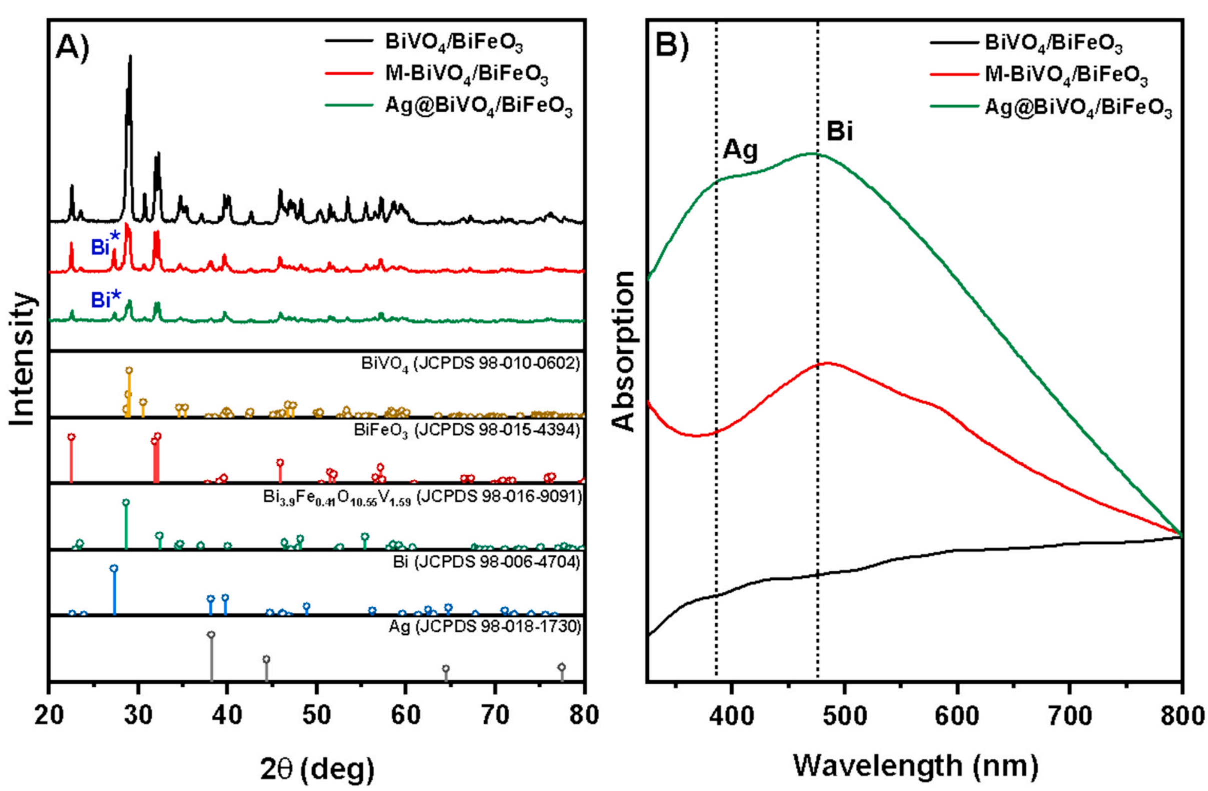

Fig. 1. (a) PXRD pattern and as well the JCPDS files and (b) UV–VIS absorption spectra of the (—) $BiVO_4/BiFeO_3$, (—) M−$BiVO_4/BiFeO_3$ and (—) Ag@$BiVO_4/BiFeO_3$.

formation of metallic bismuth. Other studies already reported the mechanochemical formation of metallic Bi NPs for similar oxides [29], although most of the metallic Bi NPs synthesis reported are solution and temperature based [30,31].

The materials were deposited over ITO glasses (indium tin oxide), as thin films and the absorption spectra recorded, Fig. 1**b**. The pristine material, $BiVO_4/BiFeO_3$, does not present any absorption bands between 350 and 500 nm. For the M−$BiVO_4/BiFeO_3$ a broad band is observed, peaking at 483 nm related to the bismuth LSPR. The Ag@$BiVO_4/BiFeO_3$ presents a new band at 380 nm corresponding to the LSPR of Ag NPs. These values agree with those reported in the literature for the bismuth and silver nanoparticles [32,33]. The plasmon bands are closely affected by the shape and size of nanoparticles [34,35]. In fact, the plasmon band of Ag NPs have a stronger relation with the size, as reported by Lee, Kiba and coworkers, which observed that as the size decreased the absorption spectra tends to blue-shift for wavelengths lower than 400 nm [36,37]. Thus, it is expected that our AgNPs present in the material to be smaller than 5 nm.

The band gap of the materials was also estimated through Tauc plot after Kubelka-Munk function by UV–VIS diffuse reflectance, (**Fig. S1**). The data reveals a decrease around 0.1 eV for the band gap of Ag@$BiVO_4/BiFeO_3$ and M−$BiVO_4/BiFeO_3$ in relation to the pristine $BiVO_4/BiFeO_3$. It can be partially explained due to the presence of metallic domains of bismuth and silver. Moreover, during the synthesis through mechanochemistry some defects can be generated in the catalyst structure, which can enhance the charge separation. It occurs because the defects act as electron trap reflecting in a lower band gap energy [38,39].

The morphology of materials was investigated through scanning electron microscopy (SEM) and transmission electron microscopy (TEM), Fig. 2. In Fig. 2**a**, it is possible to observe a formation of uniform rice-like structures for the pristine $BiVO_4/BiFeO_3$ with sizes around 1 μm, similar to those reported by Yuan [19]. For the Ag@$BiVO_4/BiFeO_3$, Fig. 2**b**, the uniform pattern in the structure is lost, producing small plates with sizes lower than 1 μm and irregular shapes as result of the milling procedure [40]. TEM images of Ag@$BiVO_4/BiFeO_3$, Fig. 2**c** and Fig. 2**d**, show a uniform distribution of roundish nanoparticles over the oxides, with average size around 7 ± 2 nm. The measured interplanar spacing reveals a *d*-spacing of 0.372 nm, corresponding to the interplanar distance of (101) planes of metallic bismuth (JCPDS 98–018-1730). Energy dispersive X-ray spectroscopy analysis in STEM mode (STEM-EDX) was then carried out for mapping the elemental distributions in the sample, Fig. 2**e** and (**Fig. S2**). The distribution of Bi, V, and Fe have a uniform pattern over a 20 nm site. Silver islands (5 – 15 nm) over the oxides could be finally identified, in addition to a highly dispersed form of Ag over the material. Furthermore, an EDX semi-quantitative analysis on this site reveals that the amount of Ag on this site corresponds to 4.57 % in mass, which agrees with the AAS values obtained.

X-ray photoelectron spectroscopy (XPS) analyses were carried out to probe the surface of the samples prior to electrochemical tests, Fig. 3. The survey spectra indicate the presence of all the expected elements (**Fig. S3-S4**). The XPS spectrum of the pristine mixed oxide, i.e., the $BiVO_4/BiFeO_3$, Fig. 3**a**, display doublets in the region of Bi 4f transitions, peaking between 166 – 160 eV [41]. The deconvolution of these signals shows two pairs of doublets at 159.4/164.7 eV and 160.6/165.9 eV

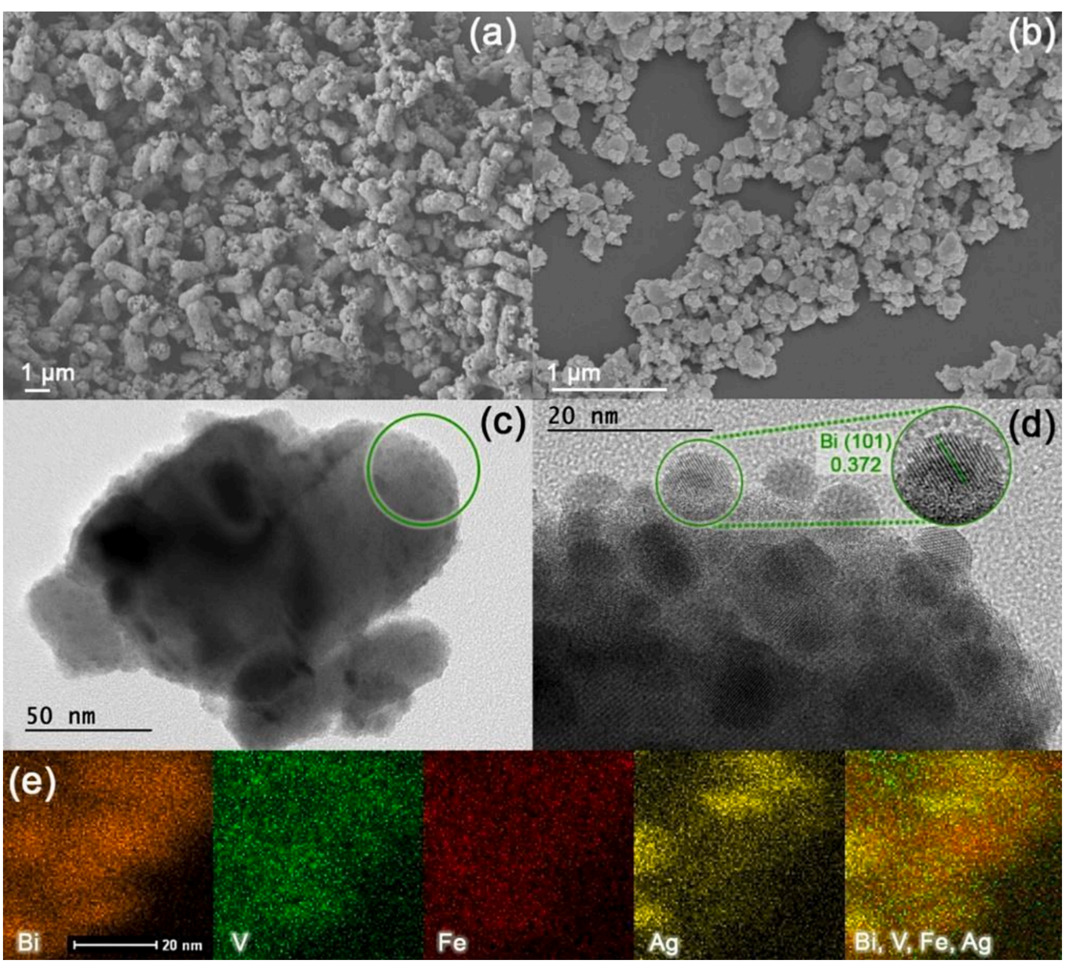

Fig. 2. SEM images for (a) $BiVO_4/BiFeO_3$, (b) Ag@$BiVO_4/BiFeO_3$, TEM images for (c) Ag@$BiVO_4/BiFeO_3$ (d) zoom of nanoparticles over Ag@$BiVO_4/BiFeO_3$ with the interplanar distance and (e) STEM-EDX mapping for Ag@$BiVO_4/BiFeO_3$.

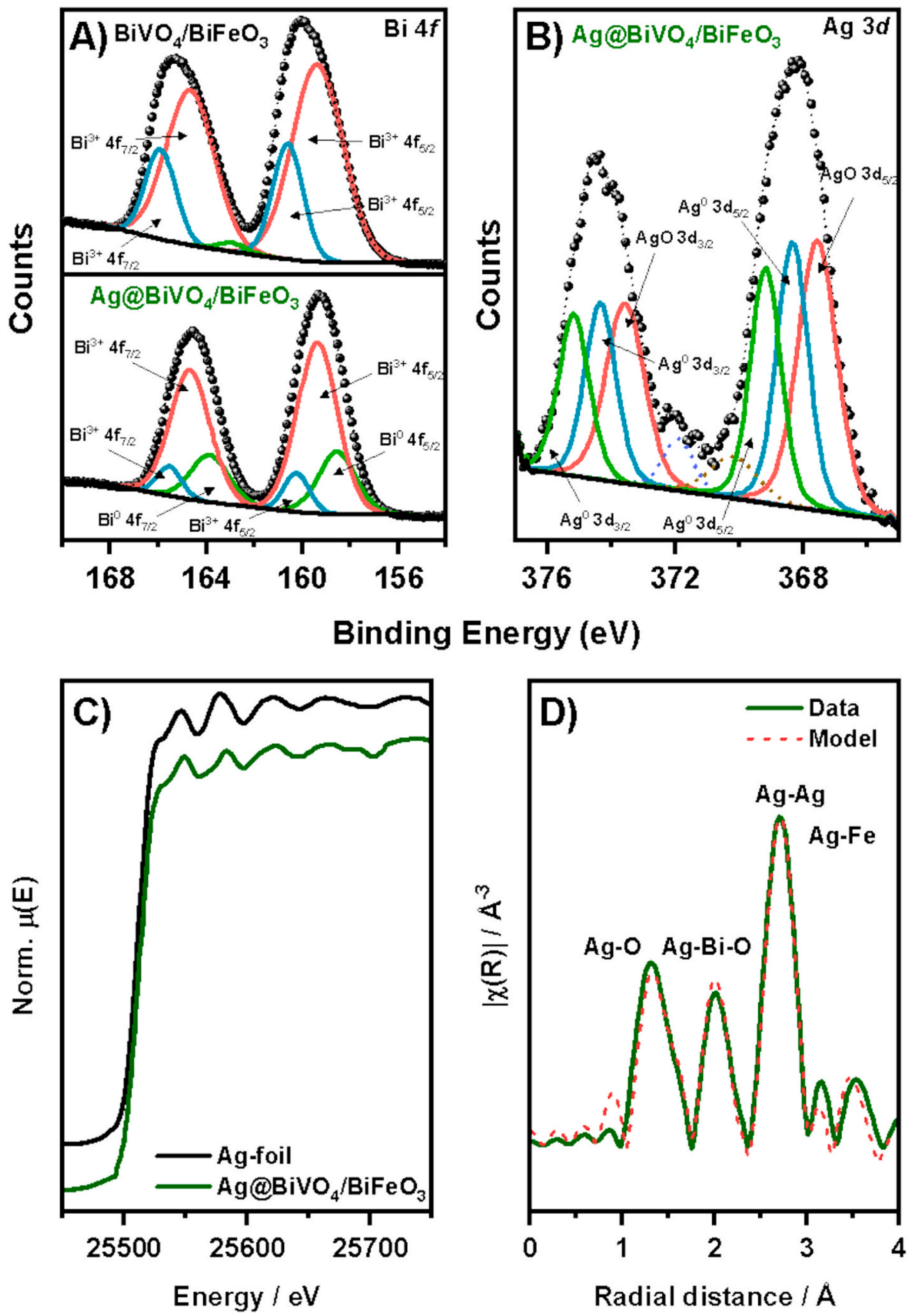

Fig. 3. XPS spectra of pristine $BiVO_4/BiFeO_3$ and milled Ag@$BiVO_4/BiFeO_3$ (A) bismuth and (B) silver assignments, (C) Ag K-edge XANES spectra of Ag-foil and Ag@$BiVO_4/BiFeO_3$ and (D) Fourier Transformed Ag-K edge k^2-weighted EXAFS spectra of Ag@$BiVO_4/BiFeO_3$.

(Bi^{3+} $4f_{7/2}$ / Bi^{3+} $4f_{5/2}$) separated by 5.3 eV, assigned to $BiFeO_3$ and $BiVO_4$ [42,43]. A more complex Bi 4f signal is found for the Ag@$BiVO_4$/$BiFeO_3$ sample. The deconvolution shows the same signals relative to the Bi^{3+} $4f_{7/2}$ and Bi^{3+} $4f_{5/2}$ from both semiconductors, $BiVO_4$ and $BiFeO_3$. However, a new Bi 4f doublet is observed in a lower BE at 158.5 eV and 163.9 eV, when compared to the oxidized species of Bi^{x+}. The shift to lower BE involves the contribution of other bismuth oxides such as Bi_2O_3 due to Bi^0 NPs surface oxidation [44,45], but it could also encompass the presence of metallic bismuth nanophase [46], corroborating the results of PXRD, TEM and UV–VIS spectroscopy. The electronic transition relative to Ag 3d were also probed for Ag@$BiVO_4/BiFeO_3$, Fig. 3**b**. The data treatment of the of Ag 3d XPS spectrum was also challenging, but the use of appropriate constrains for peak fitting, including FWHM, and the results from UV–VIS, showing the LSPR of AgNPs, enable us to assign the presence of metallic silver in two pairs of doublets **(further details in SI)**. The first doublet centered at 368.4 and 374.4 eV, relative to Ag $3d_{5/2}$ and Ag $3d_{3/2}$ transitions respectively, is consistent with the BE of Ag^0 of bulk or extended Ag nanoparticles and the second, centered at 369.2 and 375.2 eV, indicates the presence of smaller AgNPs domains [47,48]. This result complements the EDX-STEM (Fig. 2**e**), where silver could be seen either as larger agglomerates and finely dispersed over the mixed oxides. In addition, the transitions of lower BEs relative to metallic silver, peaking at 367.6 and 373.6 eV, can be attributed to oxidized Ag, probably AgO ($Ag^{1+/3+}$) on the AgNPs surface [49]. Finally, two bumps are found around 370.3 and 371.8 eV, that could not be distinguished from artifacts or a $Ag^{x+}3d_{5/2}$ satellite peak [49].

The XPS spectra for V $2p_{3/2}$, V $2p_{1/2}$, Fe $2p_{3/2}$ and $2p_{1/2}$ show small shifts to higher BEs for the material containing silver, indicating changes in the oxidation state of these species **(see SI)**. The shifts in BEs for V $2p_{3/2}$, V $2p_{1/2}$, Fe $2p_{3/2}$ and $2p_{1/2}$ can be attributed to the generation of oxygen vacancies as well as to the partial reduction of iron and vanadium in the catalyst's structure [42].

To obtain more information concerning silver in the structure of Ag@$BiVO_4$/$BiFeO_3$, X-ray absorption near edge structure (XANES) and extended X-ray absorption fine structure (EXAFS) measurements were carried out, Fig. 3**c** and **d**. Fig. 3**c** displays the Ag K-edge XANES spectra of the sample and a reference Ag foil. When compared to the standard metallic silver foil, the XANES spectra of our material shows no edge shift (both at 25,514 eV), therefore, confirming the metallic nature of mostly of the silver in the material. The dispersion of silver was further investigated by EXAFS. The magnitude of the Fourier transformed spectrum of the sample is displayed in Fig. 3**d** as a function of the radial distribution with respect to the absorbing element (for further details about EXAFS, as well the real, imaginary parts as well as in *k*, **see SI**). Similarly, as the above discussed PXRD and XPS, the heterogeneity of the material made it very complex to find a representative model for the Ag local structure. Nonetheless, we succeeded in modeling the silver distribution considering both metallic and silver oxides, which included mixed oxides of silver with iron or bismuth **(details in SI)**. In Fig. 3**d** we can distinguish three main peaks. The first two around 1.4 and 2.0 Å have the contribution of Ag-O scattering in AgO and Ag-Bi-O double scattering in AgBiOx, respectively. The most intense peaks around 2.8 Å englobes the contribution of Ag-Ag scattering, typical of Ag^0 in small cluster and NPs [50,51]. Also, the is a small contribution of Ag-Fe scattering. Overall, the results of EXAFS, indicates the stressed and high distorted structure of Ag@$BiVO_4$/$BiFeO_3$ originated from its mechanochemical preparation. As the milling process can introduce defects in the catalysts structure, especially in the presence of a reductant such as $NaBH_4$, Mott-Schottky plots analysis was performed, allowing to estimate the extension of defects based on the changes in the charge carriers' density. Then, impedance experiments were carried out in the capacitive potential range and the plots were constructed through the following equation, **Eq. (1)** [52].

$$\frac{1}{C^2} = \frac{2}{\varepsilon\varepsilon_0 A^2 e N_d}\left(V - V_{fb} - \frac{k_B T}{e}\right) \tag{1}$$

The terms of equation correspond to, C the differential capacitance, ε dielectric constant of the semiconductor ($BiVO_4$ = 86 and $BiFeO_3$ = 53) [43,53], ε_0 vacuum electric permittivity, A area, e elemental charge, N_d charge carriers' density, V applied potential, V_{fb} *flatband* potential, k_b Boltzmann constant and T temperature. The Mott-Schottky plots for all materials exhibit two linear regions along the different potentials, Fig. 4. The first region, with a positive slope, corresponds to the $BiVO_4$ and the second one with a negative slope to the $BiFeO_3$[19], commonly observed for p-n heterojunctions in semiconductors [54]. The slope of the linear regions was used to estimate the charge carriers' density (N_d). In the pristine material, $BiVO_4$/$BiFeO_3$, the N_d achieved have a magnitude in the order of 10^{21} in both linear regions. For M−$BiVO_4$/$BiFeO_3$ material, the increase of N_d occurs mainly in the range related to the $BiVO_4$, with N_d values more negative than the pristine material $BiVO_4$/$BiFeO_3$. To the Ag@$BiVO_4$/$BiFeO_3$, the increase of N_d occurs at the same extension for both semiconductors, $BiVO_4$ and $BiFeO_3$. The N_d values achieved for Ag@$BiVO_4$/$BiFeO_3$ are one order of magnitude (10^{20} for $BiVO_4$ and 10^{22} for $BiFeO_3$) in relation to the pristine material $BiVO_4$/$BiFeO_3$. The N_d values achieved for the Ag@$BiVO_4$/$BiFeO_3$ revealed that the presence of silver species induces the increase of charge carriers in both semiconductors, a fact which is not observed for M−$BiVO_4$/$BiFeO_3$. Interestingly, the increase of charge carriers' density agrees with the shift to lower BE for V $2p_{3/2}$ and V $2p_{1/2}$ in XPS, that could be related to an increase of oxygen vacancies in the structure and respective change in the oxidation state of V for charge compensation. The presence of defects in the structure is a good approach to improve the gas adsorption over the catalysts surface for different reactions [55–58].

3.2. Plasmon-enhanced electrocatalysis

The electrocatalytic properties of the Ag@$BiVO_4$/$BiFeO_3$ were evaluated by Linear Sweep Voltammetry (LSV). The experiments were carried out in 0.2 mol L^{-1} $KHCO_3$ under saturated atmosphere of Ar, N_2, CO_2 and in the mixture of N_2 + CO_2 at 10 mV s^{-1}, Fig. 5**.**

3.2.1. Absence of light (dark)

Concerning initially the electrochemical properties of Ag@$BiVO_4$/$BiFeO_3$ in absence of light, Fig. 5**a**, under Ar atmosphere it is possible to observe that the current density increase along with the potential, starting around −0.1 V *vs* RHE reaching an abrupt increasement after −0.4 V *vs* RHE. Under such atmosphere conditions and potential range, the only possible reaction is associated with the hydrogen evolution reaction (HER). Considering the experiments under N_2 atmosphere, the current density raise after −0.4 V *vs* RHE, which is associated to the adsorption to the N_2 over the catalyst and consequently its activation according to Brito and colleagues [11]. When the electrolyte is saturated with CO_2, the current density starts to increase at lower potentials, such as 0.0 V *vs* RHE. For the experiment performed under N_2 + CO_2 (1:1) atmosphere, a higher current density is achieved at the same potential, −0.1 until −0.4 V *vs* RHE, when compared to the Ar, N_2 and CO_2 atmospheres. The behavior observed under N_2 + CO_2 suggests a synergism between the activation of both species prior to the C-N coupling. Comparing the results for Ag@$BiVO_4$/$BiFeO_3$ under N_2 + CO_2 to the electrochemical profile reported by Yuan and collaborators for $BiVO_4$/$BiFeO_3$ some differences can be observed [19]. Yuan observed that under N_2 + CO_2 the current density starts to increase around −0.3 V *vs* RHE, while in this work it is observed around −0.1 V *vs* RHE. This potential displacement behaviour accords to other studies reported in which the changes in the charge carriers' density, can result in an improvement of the interaction between the catalyst and species of interest, N_2 + CO_2 [59]. Our results demonstrated that the changes in the charge carriers' density, *e.g.* the oxygen vacancies formation, can result in such improvement, reflecting in the reduction of the overpotential necessary to activate the N_2 and CO_2 species.

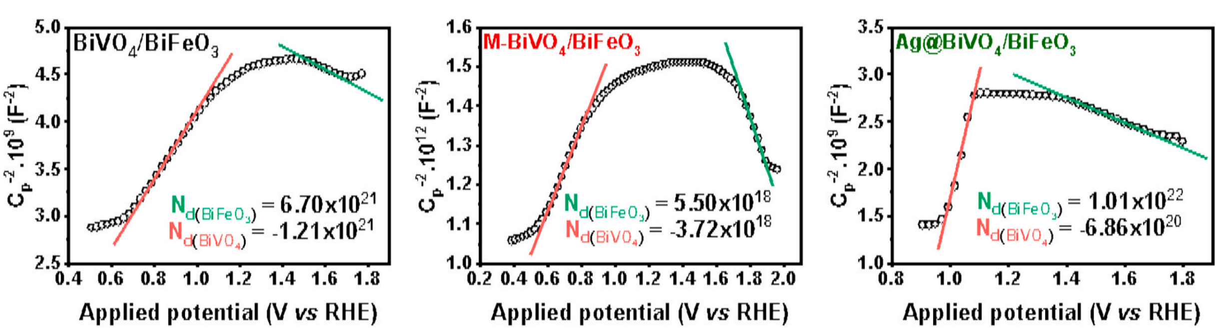

Fig. 4. Mott-Schottky plots for (a) $BiVO_4$/$BiFeO_3$ pristine (b) M-@$BiVO_4$/$BiFeO_3$ and (c) Ag@$BiVO_4$/$BiFeO_3$ at 100 Hz in 0.2 mol L^{-1} $KHCO_3$.

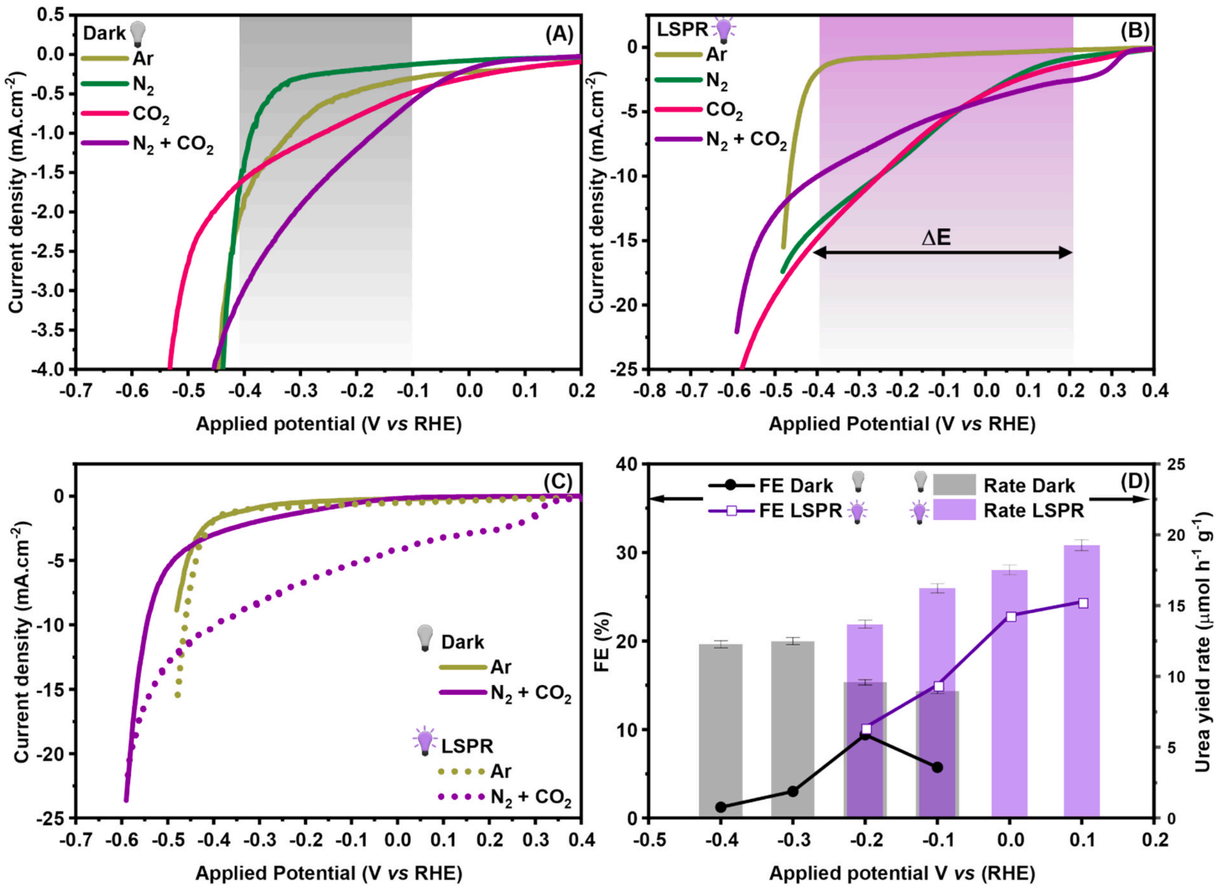

Fig. 5. Linear Sweep Voltammetries of Ag@$BiVO_4$/$BiFeO_3$ in 0.2 mol L^{-1} $KHCO_3$ at 10 mV s^{-1}, (a) in absence of light (dark), (b) under LSPR conditions (laser irradiation, λ = 455 nm and 1 W cm^{-2}), (c) comparison between dark and laser irradiation, (d) Faradaic efficiencies and urea yield rates after bulk electrolysis (2 h) at different potentials under N_2 + CO_2.

3.2.2. LSPR conditions (laser irradiation)

Under LSPR conditions, that is laser irradiation, Fig. 5**b**, and considering Ar atmosphere, no significant changes in the current density, or even in the potential window, were observed. On the other hand, in saturated electrolyte with N_2, CO_2 and N_2 + CO_2 gases it is possible to observe an increase in current in a wider potential window of around 600 mV, starting from + 0.2 V to −0.4 V *vs* RHE. Furthermore, for the solely gases, N_2 and CO_2, the current density rises in the same extension for both atmosphere conditions. The electrochemical profiles under LSPR, also show a sharp increase in the current density which indicated that at such condition the catalyst effectively participates on the interaction and consequently activation of N_2 and CO_2 species for the C-N coupling.

The comparison of the electrochemical profiles in the absence of light and LSPR conditions, Fig. 5**c**, allows important comparisons. Under LSPR conditions, the potential window increases, as well as the current density, in relation those within absence of light. The values achieved under LSPR conditions turn around 10 mA cm^{-2} at −0.4 V *vs* RHE, contrasting with the 2.5 mA cm^{-2} at the same potential in absence of light. It reveals that the expansion of potential range and current density is not exclusively related to the presence of NPs in the catalyst structure. In this case, the LSPR phenomena boosts the interaction between the catalyst and N_2 and CO_2 species and consequently their activation, suppressing the interaction with water molecules that could lead the HER as side reaction.

3.2.3. Bulk electrolysis

Bulk electrolysis experiments were carried out in an H-cell in the absence of light and at LSPR conditions, considering N_2 + CO_2 as atmosphere. Urea detection e quantification was carried out by ^{1}H NMR and colorimetric test based on the diacetyl-monoxime method **(see SI)** [59]. The experiments were carried out for 2 h under constant purge of N_2 + CO_2 and aliquots from catholyte were collected before and after electrolysis. Firstly, aliquots from catholyte were analyzed by ^{1}H NMR before and after electrolysis and compared with a urea standard. The data reveal that before electrolysis no signals correspondent to urea are observed in ^{1}H NMR spectra **(see SI)**. After 2 h of electrolysis a relative signal at 5.45 ppm is observed for all potentials tested. During electrolysis under LSPR conditions, the temperature of the electrochemical cell and electrode surface were also monitored by a thermal camera (FLIR ETS 320) and no significant changes in the temperature mapping were observed **(Fig. S13 see SI).**

The Faradaic Efficiency and urea yield rate was calculated after 2 h of electrolysis as a function of the applied potential, Fig. 5**d**. In the absence of light, urea yield rate raises as the applied potential increases, reaching values ranging from 8.9 to 12.5 μmol h^{-1} g^{-1}. The maximum FE obtained pivots around 9.4% at −0.2 V *vs* RHE, which readily decreases as the potential increases.

Upon LSPR conditions, the urea yield rates, and the FE decreases as the potential increases with values ranging from 13.7 to 19.2 μmol h^{-1} g^{-1}, which are almost two times higher than those attained in the absence of light. Such behavior is explained due to the possibly preferential HER at higher potential. The FE in LSPR conditions reaches a maximum of 24.4% at +0.1 V *vs* RHE. Comparing the values obtained at the same potential, −0.1 V *vs* RHE in the absence of light and under LSPR conditions, the LSPR effect become evident as both FE and urea yield raise almost 50%. Furthermore, under LSPR conditions, both the catalytic activity and structural integrity of Ag@$BiVO_4$/$BiFeO_3$ are preserved for over 10 h (**see Fig. S14 of SI**). Our FE values obtained are consistent with those reported of Yuan and collaborators for the bare $BiVO_4/BiFeO_3$ [19]. In their study the maximum FE achieved for bare $BiVO_4/BiFeO_3$ was 17.18 % at −0.4 V *vs* RHE, while for the Ag@$BiVO_4$/$BiVO_4$ the maximum achieved was 24.4 % at +0.1 V *vs* RHE. In fact, it reveals that slight modifications in the catalyst structure associated with the plasmon-assisted effect tune the selectivity improving the urea yield.

Considering the aspects involving the N_2 and CO_2 co-electrolysis, it is clear that the activation of species must occur in the same extension and at lowest possible overpotential to avoid HER. As the potential increases, the HER becomes a strong side reaction, which has already been proved to be facilitated kinetically and thermodynamically towards the N_2 and CO_2 reduction [60,61]. The result of different potentials applied for the gas species activation results in volcano plots for FE, in which there is an optimal potential in which the N_2 reduction occurs at the same extension as the CO_2, followed by HER [62]. Regarding the Ag@$BiVO_4/BiFeO_3$ catalyst in the absence of light, this trend is followed since the maximum FE occurs at −0.2 V *vs* RHE and readily decreases as the potential increases. It suggests that along the potential increase, the HER competes with the electrochemical C-N coupling. Under LSPR conditions, as observed by bulk electrolysis data, the potential in which N_2 and CO_2 are reduced are lower than those in dark conditions and occur at the same extension. This behavior is also confirmed by LSV results showing that upon LSPR conditions, the catalyst promotes the activation of both species in similar potentials. As result of it, higher values for FE and urea yield rates are achieved compared to those in the absence of light.

Aiming a better understanding of how LSPR can enhance the electrochemical C-N coupling, promoted by the catalyst, Mott-Schottky plot analysis and photocurrent experiments were also employed to observe the behavior of the material under different atmospheres and laser exposure, Fig. 6**.**

In the Mott-Schottky plots for Ag@$BiVO_4/BiFeO_3$, Fig. 6**a**, it is possible to observe that the *flatband potential* (V_{fb}) changed as a function of the atmosphere and LSPR excitation. The difference between the V_{fb} in absence of light under Ar and $N_2 + CO_2$ is −100 mV. Considering the LSPR conditions and $N_2 + CO_2$ atmosphere, the difference is even more pronounced, with a difference of −300 mV when compared to $N_2 + CO_2$ in the absence of light. It suggests that under LSPR conditions, the lifetime of the charge carriers in the presence of $N_2 + CO_2$ is lower than in the other conditions resulting in a lower reactive capacitance towards charge recombination [63]. The changes observed in the *flatband potential* also confirm the behavior observed in the LSVs under different atmospheres and in the absence of light and under LSPR conditions.

Experiments of photocurrent were also conducted for all the materials to distinguish between the possible photoelectrochemical effect of semiconductor and LSPR effect of nanoparticles. The pristine material, $BiVO_4/BiFeO_3$ at chopped laser irradiation (λ = 455 nm) in both the atmosphere conditions of Ar and $N_2 + CO_2$ **(SI)**, did not present any signals. In the experiments using M−$BiVO_4/BiFeO_3$ under $N_2 + CO_2$, no evident signal is observed at 0.0 V *vs* RHE, starting to be evident only at −0.2 V *vs* RHE, Fig. 6**b**. In other hand, for the Ag@$BiVO_4/BiFeO_3$, there is a pronounced photo response under chopped irradiation in $N_2 + CO_2$ atmosphere in both potentials, achieving stable current densities around 3 and 3.5 mA cm^{-2}. For the same material, Ag@$BiVO_4/BiFeO_3$ in Ar atmosphere, no evident signals were observed, resulting only in a noisy signal (**Fig. S15**).

The comparison of the photocurrent experiments between the pristine $BiVO_4/BiFeO_3$ and Ag@$BiVO_4/BiFeO_3$ show that the photoinduced

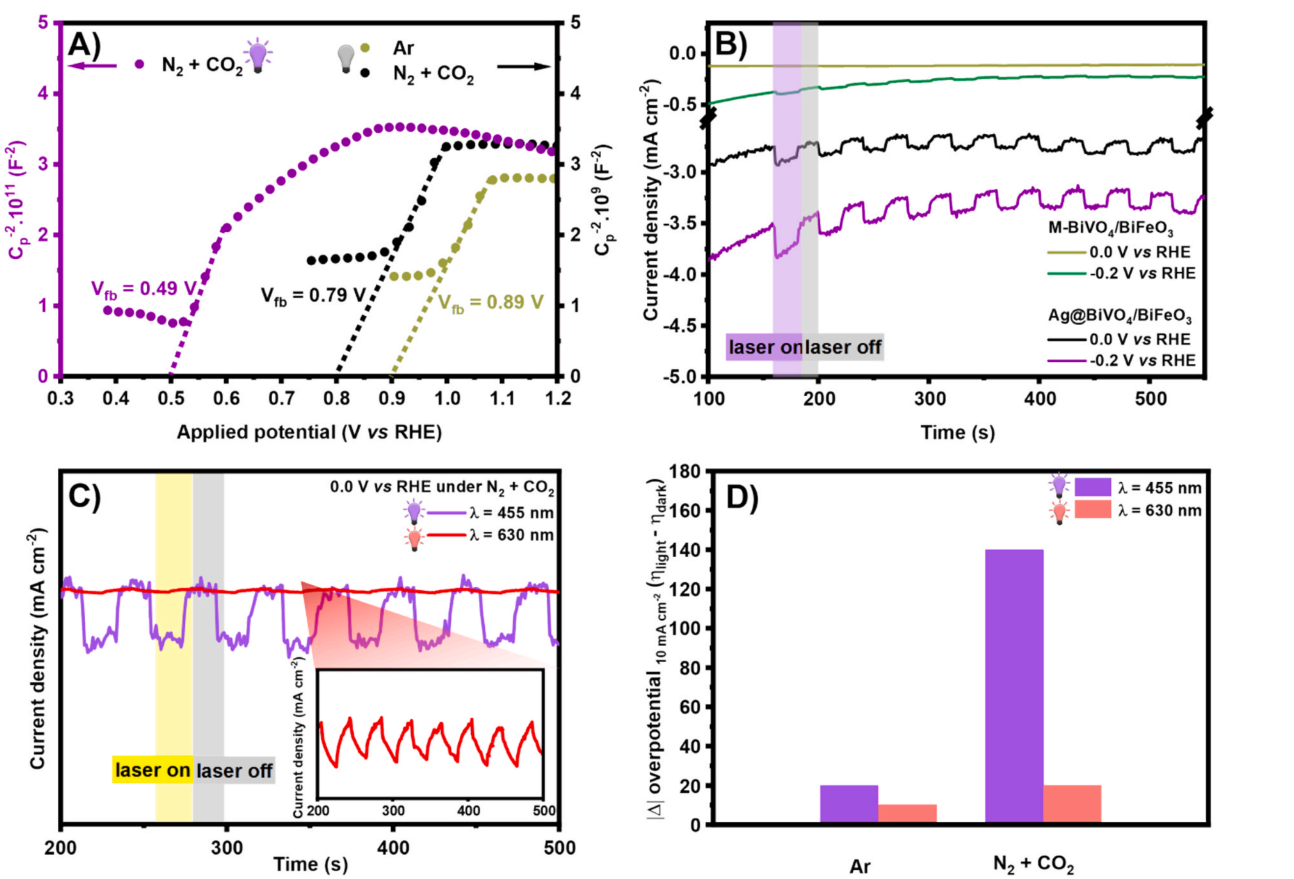

Fig. 6. (A) Mott-Schottky plots for Ag@$BiVO_4/BiFeO_3$ at 100 Hz under Ar and $N_2 + CO_2$ atmospheres considering the absence of light and LSPR condition (λ = 455 nm and 1 W cm^{-2}), (B) photocurrent analysis of M−$BiVO_4/BiFeO_3$ and Ag@ $BiVO_4/BiFeO_3$ in 0.2 mol L^{-1} $KHCO_3$ under $N_2 + CO_2$ atmosphere, (C) Photocurrent analysis of Ag@$BiVO_4/BiFeO_3$ under chopped irradiation under $N_2 + CO_2$, (zoom photocurrent analysis at λ = 630 nm) and (D) bar graph depicting the wavelength-dependent |Δ| in overpotentials ($\eta_{light} - \eta_{dark}$) at different wavelengths, λ = 455 and λ = 630 nm (1 W cm^{-2}), in 0.2 mol L^{-1} $KHCO_3$ under Ar and $N_2 + CO_2$.

effect is related to the LSPR effect of metal NPs and not attributed to a photoelectrochemical effect from semiconductors. As both Ag and Bi NPs can be responsible for LSPR effects, comparing the photocurrent results of M−$BiVO_4$/$BiFeO_3$ and Ag@$BiVO_4$/$BiFeO_3$ it is possible to distinguish the major contributors, Fig. 6**b**. Even irradiating at the bismuth plasmon band, the major LSPR effect contribution is more pronounced due to the silver nanoparticles at Ag@$BiVO_4$/$BiFeO_3$. Interestingly, for the Ag@$BiVO_4$/$BiFeO_3$ the signals are only observed under N_2 + CO_2, which reveals that photo response is closely related to the interaction of the catalyst and gas species following its consequent activation. Such behavior reveals the major contribution to the C-N coupling is related to the Ag NPs.

Experiments were also performed at different wavelengths to gain more insights about the LSPR effect, as it can result in different local effects, like the increase of local temperature, near field enhancement and generation of hot carriers. The photocurrent experiments for Ag@$BiVO_3$/$BiFeO_3$ were also performed under irradiation at λ = 630 nm and compared with the data at λ = 455 nm, Fig. 6**c**.

The photocurrent response under chopped irradiation at λ = 455 nm shows a square shape signal, while at λ = 630 nm a curve shape of much lower intensity, is observed. The square shape signal at λ = 455 nm, i.e. in the region of LSPR of AgNPs, is observed instantaneous as the laser is turned on. When the laser is turned off, the current density promptly decreases, such behavior suggests that the major contribution is related to the generation of hot carriers, although the other effects cannot be completely discarded. In fact, this behavior agrees with other reports in the literature, in which the hot carriers have lifetimes on picosecond scale [64–66]. On the other hand, at λ = 630 nm, i.e. far from the absorption band of the AgNPs, the photothermal effect is predominantly. The photothermal effect affects the mass transportation on the system and, as a result, a small and constant increase of current is observed [67–70].

The LSPR effect can be also confirmed comparing the difference between overpotential under dark and laser conditions |Δ| at different atmospheres, Fig. 6**d**. Concerning initially the Ar atmosphere conditions, the overpotential necessary to reach 10 mA cm^{-2} are 10 mV and 20 mV for λ = 630 nm and λ = 455 nm, respectively. As in Ar atmosphere the only probably reaction is HER, in this case the LSPR does contribute to the improve HER. Otherwise, when N_2 + CO_2 atmosphere is considered, the |Δ| achieved are 20 mV and 140 mV, for λ = 630 nm and λ = 455 nm, respectively. The |Δ| achieved under N_2 + CO_2 atmosphere confirms that the LSPR excitation led to the gas reduction at relatively lower overpotentials improving the selectivity of the Ag@$BiVO_4$/$BiFeO_3$ catalyst. Moreover, irradiating far from the LSPR absorption band (λ = 630 nm), the photothermal effect do not contribute for the reduction of the overpotential for the N_2 + CO_2 activation as can be observed by the lower |Δ|.

3.3. Mechanisms of N_2 and CO_2 coupling

Concerning the possible species involved in the N_2 + CO_2 co-electrolysis and the possible LSPR effects, *in situ* Fourier-Transform Infrared Reflection Absorption Spectroscopy (FTIR-RAS) experiments were performed to investigate the catalyst/electrolyte interface. *In situ* FTIR-RAS experiments were carried out under Ar and N_2 + CO_2 atmospheres in the absence of light and under LSPR conditions (λ = 455 nm). The signals were recorded in a spectral window between 4000 and 1000 cm^{-1}, Fig. 7 and **Fig. S17** from SI.

3.3.1. Ar atmosphere

Under Ar atmosphere, Fig. 7a and 7b, in both conditions, that is, in absence of light and upon LSPR conditions, no signals related to

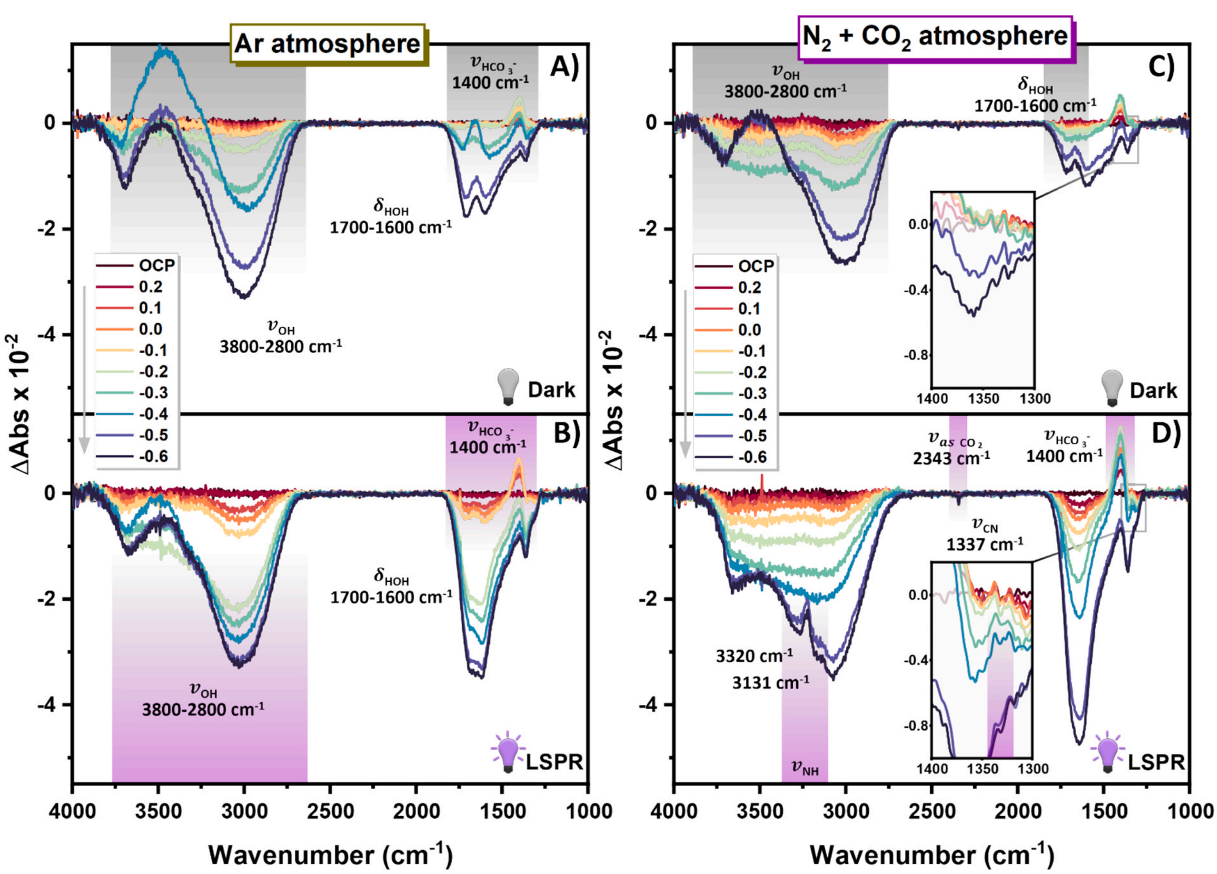

Fig. 7. *In situ* FTIR-RAS experiments under Ar atmosphere (a) in the absence of light and (b) under LSPR conditions, N_2 + CO_2 atmosphere (c) in the absence of light and (d) under LSPR conditions (laser irradiation λ = 455 nm) using Ag@$BiVO_4$/$BiFeO_3$ as catalyst in 0.2 mol L^{-1} $KHCO_3$, ΔE = 0.1 V, from OCP to −0.6 V *vs* RHE.

nitrogen-content species being formed were observed as expected. Although, different spectral profiles can be observed considering the different light conditions. The differences remain in the stretching and bending signals related to water and bicarbonate species.

In the absence of light, Fig. 7**a**, it is possible to observe that as the potential increases from OCP until −0.3 V *vs* RHE, negative increments occur in the signals between 1700 – 1600 cm^{-1} and positive increments at 1400 cm^{-1} which are related to the δ_{HOH} (water) and ν_{HCO3-} (bicarbonate) respectively. By contrast, as the potential increase even more from −0.4 V until −0.6 V *vs* RHE, the opposite behavior is observed, in which the δ_{HOH} signals starts to have a positive increment while ν_{HCO3-} a negative one. Furthermore, at this potential range, positive signals are observed around 3800–2800 cm^{-1} related to the ν_{OH} (water) stretching from water species. This behavior under dark conditions suggests that at lower potentials (below −0.3 V *vs* RHE) initially occurs the adsorption of HCO_3^- species over the catalyst surface. Then, as the potential increased over −0.4 V *vs* RHE, water molecules started to adsorb over the catalyst surface.

Regarding the experiments under LSPR conditions, Fig. 7**b**, as the potential increases from OCP to −0.3 V *vs* RHE, it is possible to observe a negative increasement in 1700 – 1600 cm^{-1} related to δ_{HOH} signal, and around 1400 cm^{-1} (ν_{HCO3-}), a positive one. As the potential increases from −0.4 to −0.6 V *vs* RHE, the signals related to the HCO_3^- remain unchanged positively. However, the signals related to the ν_{OH} and δ_{HOH} from water starts to increase positively, but the last one, δ_{HOH}, lies in the intensity. In fact, under LSPR conditions and lower potentials, it is possible to observe that most water molecules do not easily adsorb onto the catalyst surface. Such behavior contrasts with the results in the absence of light, in which water molecules are easily adsorbed. This pattern explains the reason that in the LSVs experiments under Ar atmosphere (Fig. 5**a, b** and **c)** no significant changes in the current densities were observed before reaching −0.4 V *vs* RHE under both conditions, absence of light and upon LSPR. Furthermore, in the previous section, we reported that under Ar atmosphere (**Fig. S15**) no photocurrent response signals were observed at the studied potentials, 0.0 V and −0.2 V *vs* RHE. Since under Ar atmosphere, the only possible reaction to result in an increase in the photocurrent experiments is HER, in the studied potentials no electrochemical reaction is observed. Based on it, both LSVs and photocurrent response experiments, agrees with *in situ* FTIR-RAS in which the amount of water over the electrode surface seems to be limited. As result of the management of water in the catalytic surface the HER is suppressed.

3.3.2. $N_2 + CO_2$ atmosphere

The *in situ* FTIR-RAS experiments were also carried out under $N_2 + CO_2$ atmosphere in the absence of light and upon LSPR conditions. Focusing initially on the absence of light condition, Fig. 7**c**, the signals related to the ν_{OH}, δ_{HOH} and ν_{HCO3-}, follows the same trend observed under Ar atmosphere, that is, as the potential increases from OCP until −0.3 V *vs* RHE, negative increments occur in the signals between 1700 – 1600 cm^{-1} and positive increments at 1400 cm^{-1} which are related to the δ_{HOH} and ν_{HCO3-} respectively. This observation confirms that in the absence of light and this potential window, the adsorption of water in the catalyst surface is not facilitated. In relation to the formation of nitrogen-rich species in the absence of light, no huge signals are observed as expected. Actually, around 1337 cm^{-1} a signal related to the ν_{CN} stretching can be observed, although it lies in the intensity.

Under LSPR conditions, Fig. 7**d**, and considering the potential window from OCP until −0.4 V *vs* RHE, it is possible to observe a signal at 1337 cm^{-1} increasing along the potential related to the ν_{CN} band. Between −0.5 V and −0.6 V *vs* RHE, it is possible to observe positive signals at 3320 and 3131 cm^{-1} related to ν_{NH}. Furthermore, at 2343 cm^{-1} signals related to the ν_{CO2} are observed. The signals observed for the ν_{CN} and ν_{NH} are in agreement with other reports in the literature for urea electrosynthesis [16,71].

Considering the aforementioned aspects, the absence of clear signals or other nitrogen-rich species in the absence of light can be explained by the high competition for the active sites of the catalysts by water, bicarbonate, N_2 and CO_2 species. As a result of it, small amounts of urea are produced at the electrode surface giving signals which lie in the intensity. Moreover, the values obtained for FEs and urea yields rates in absence of light reflect this behavior. In addition to it, this behavior also agrees with the LSVs profiles under absence of light, Fig. 5**a**, in which there is not a clear tendency in the activation of species based on the changes of the current density. Otherwise, upon LSPR conditions the signals for nitrogen-rich species and urea through the ν_{CN} are evident and match with the LSVs results. The ν_{CN} signal related to the urea formation, remains clear until −0.4 V *vs* RHE. According to the LSVs experiments, until this potential considering the $N_2 + CO_2$ atmosphere, there is an increase of current density which is not observed in the LSVs under Ar. Afterwards, the ν_{CN} signal is not observed even more due to the competition with water for catalytic sites that led HER; then, only signals for NH intermediates reminiscent were observed. These results completely agree with the behavior observed in the LSVs experiments in all atmosphere conditions under light irradiation.

Based on the results, it is clear that LSPR effect plays an important role during the $N_2 + CO_2$ co-electrolysis to yield urea. The overall effect that summarizes how the LSPR enhances the $N_2 + CO_2$ co-electrolysis is related to the availability of water at the catalyst surface which suppresses HER result in an improvement of selectivity. This behavior was observed in all the experiments above mentioned.

As different mechanisms can be observed as result of LSPR, as aforementioned the hot-carriers generation, enhancement of near field and increase of local temperature, is quite difficult to separate each contribution of LSPR in relation to the water control over catalyst surface. In the photocurrent response experiments under $N_2 + CO_2$ atmosphere, we tentatively attributed that the major contribution would be related to the hot-carriers generation based on the shape of curves and previously reports of literature. Although, the other effects from LSPR cannot be completely discarded.

Despite the mechanisms involving water sphere solvation, or HER suppression during LSPR being not completely understood, some reports in the literature have observed differences concerning the electrochemical aspects in the absence of light and LSPR conditions, which can be also extended to our system. McCloskey and colleagues in their study of CO_2 electrochemical reduction assisted by LSPR using Ag electrodes, observed different distribution of products along different overpotentials [72]. In the absence of light, the authors observed that hydrogen was the most predominant product, that is HER dominating over CO_2 reduction. Upon LSPR conditions the authors observed HER keeping a constant FE for hydrogen species in different potentials. As the main reason for suppression of HER, the authors pointed out that hydrogen precursor would be removed from Ag surface by desorption induced by electronic transitions (DIET) due to the hot carrier's generation on LSPR conditions [72–74]. Moreover, in a second study, McCloskey and colleagues monitored the Ag electrode surface and electrical double layer by ATR − SEIRAS (attenuated total reflectance − surface-enhanced infrared absorption spectroscopy) in 0.1 mol L^{-1} $KHCO_3$ electrolyte [75]. The study was carried out as function of the potential and illumination conditions towards CO_2 reduction. The ATR-SEIRAS spectra reveals changes in the HCO_3^- stretching promptly upon LSPR excitation along the different potentials. The authors attributed it to the increasement of the local pH resulting in the HER suppression [75]. The HER suppression can be also explained by a recent study of our group around the LSPR contributions towards the electrochemical oxygen evolution reaction on $Ni(OH)_2$ nanostructures decorated with Au NPS in different aqueous electrolytes [76]. The authors observed by photoelectrochemical experiments that relaxation of excited states from plasmonic phenomena occurs through phonon-electron and phonon–-phonon scattering of NPs [76]. As the phonon-electron and phonon–-phonon scattering can result in local heating, was observed changes in the solvation shell across the ions from electrolyte [76,77]. This proposition was also supported through FTIR-RAS by the monitoring of the δ_{HOH} of water [76]. Thus, it is important to highlight that our system can be inserted into all the mechanisms contributions previously mentioned.

3.3.3. Theoretical calculations

We also performed theoretical investigations to gain further insights into the catalyst mechanism by evaluating the adsorption energy (E_{ads}) of the starting reactants $CO_{2\ (g)}$ and $N_{2\ (g)}$ on pristine $BiVO_4$, $BiFeO_3$, and silver surfaces. For $BiFeO_3$ and $BiVO_4$, we utilized the same crystalline system and plane as described by Yuan in 2021 [19], while the 111 plane was used for silver. The results for the most stable site on each surface are presented in Table 1.

The initial adsorption process of $CO_{2\ (g)}$ is expected to occur at $BiFeO_3$ through a chemisorption mechanism involving interaction with an oxygen bridge on the surface (**Fig. S16a**). No other favorable adsorption sites were identified. In contrast, N_2 requires significant energy to interact with the $BiVO_4$ surface (**Fig. S16b**). Still, as it is lower than the subsequent steps described below, one can consider the $BiVO_4$ as a surface to bring N_2 molecules closer.

We observed experimentally that including silver reduces the electrochemical potential required for the reaction. Therefore, we aimed to create additional models incorporating silver to identify alternative initial interaction sites for CO_2 or $N_{2\ (g)}$ in its presence. Our most promising model, offering relatively low computational costs, involved a small silver cluster (Ag_4) positioned on $BiFeO_3$. In a simplified manner, this model can represent the edge of the interaction between the Ag and $BiFeO_3$ nanoparticles. Moreover, this model agrees with the XANES and EXAFS results observed in the material characterization section.

In the iron site near the Ag_4 cluster for the $BiFeO_3$-Ag_4 model, a favorable initial site for $CO_{2\ (g)}$ adsorption was identified (**Fig. 8a-b** and **Fig. S17a**), with E_{ads} of −0.18 eV. By analyzing the charge density differences, we can observe that the inclusion of the Ag_4 cluster increases the basicity of the iron site through the interaction with oxygen atoms (**Fig. S17b**). Then, the CO_2 can interact with the Fe center and the Ag_4 cluster (**Fig. S17c**). All the theoretical results below align well with the experimental findings, suggesting this model effectively describes this reaction.

To determine the most likely mechanism, we examined three possibilities based on the mechanism already described in the literature [19,74]: (1) the adsorption of N_2* onto the surface of $BiFeO_3$-Ag_4 (**Fig. S18a**), (2) a one-step process where N_2 is adsorbed and subsequently hydrogenated to form NNH* species (**Fig. S18b**), with both possibilities 1 and 2 occurring in the presence of already adsorbed CO_2*, and (3) the hydrogenation of CO_2* to produce COOH* (**Fig. 8c**). We found that the lowest N_2* adsorption energy was 1.60 eV, while the Gibbs free energy for forming NNH* and COOH* at their most stable sites were 1.67 eV and 1.33 eV, respectively. Therefore, after the exothermic CO_2 adsorption over $BiFeO_3$ – Ag_4, reducing to COOH* requires an increment of the free energy. The hydrogenation from COOH* to CO* (**Fig. 8d**) with the release of water is exergonic, with an ΔG of −1.15 eV. In contrast, N_2* adsorption (E_{ads} = 1.71 eV, **Fig. S18c**) and NNH* formation (ΔG = 0.92 eV, **Fig. S18d**) were unfavorable with COOH* adsorbed.

In our study involving *CO, we considered the possibility of *CO release, and the calculated desorption energy of 0.43 eV was obtained. Additionally, we found the adsorption energy for *N_2 to be 1.06 eV (**Fig. S18e**) and the Gibbs free energy for *NNH formation to be 0.22 eV, both in the presence of *CO adsorbed. In this scenario, the most energetically favorable pathway for forming *NNH species occurs on the $BiFeO_3$-Ag_4 catalyst, with *CO already bonded to an iron center (**Fig. 8e**). The occurrence of *NNH species is consistent with our spectroelectrochemical measurements and in many pathways to urea [78].

The C-N coupling reaction of *CO and *N_2 (or NNH) to form an *NCON (or *NCONH) intermediate is a kinetically determining factor in synthesizing urea [74]. At first, we determined the free energy for the coupling reaction to *NCONH (**Fig. 8f**), which was ΔG = 0.71 eV. To identify the transition state for this reaction, we employed the nudged elastic band method (**Fig. S10a, last step – grey line**). The initial increase in energy during this reaction over BiO_3Fe-Ag_4 is primarily due to the breaking of the Fe-CO bond. The highest free energy point, with $\Delta G^{\neq}$ = 1.80 eV, occurs when the interactions between *NNH, an oxygen bridge, and an iron center are broken (**Fig. S19a**). Bringing *CO and *NNH together for the coupling reaction requires considerable energy (∼1.30 eV) in the sequence (**Fig. S19b**). However, after forming the *NCONH species, the energy decreases as this species becomes stabilized through interactions with an iron center via a nitrogen atom and with the Ag_4 cluster through an oxygen atom (**Fig. S19c**). All steps after *NCONH usually show a downhill energy profile and were not evaluated.

To ensure we described the lowest energy pathway, the production of NNH*, NCON*, and NCONH* and the possibilities of NNH* or N_2* with CO* or CO_2* co-adsorption over the $BiVO_4$ surface were also verified and showed unfavorable energies (**Table S3**) comparable to those of the other pathways described above.

Table 1
Adsorption energies for CO_2 and N_2 at their most stable sites on the studied surfaces.

Adsorbate	$BiFeO_3$ (eV)	$BiVO_4$ (eV)	Ag (eV)	$BiFeO_3$ – Ag_4 (eV)
$CO_{2\ (g)}$	−0.54	0.54	0.71	−0.18
$N_{2\ (g)}$	1.52	0.49	0.74	–

4. Summary

Based on the results presented in the previous sections and considering the recent reports of different catalysts for the N_2 and CO_2 co-electrolysis to yield urea, Table 2, some inferences can be done.

The entries presented in Table 2 demonstrate that both the nature of the catalysts and the operating conditions play crucial roles in N_2 and CO_2 co-electrolysis. Regarding the catalyst composition, our mechanochemical synthesis approach for Ag@$BiVO_4$/$BiFeO_3$ results in a material that operates at a significantly lower overpotential (−0.2 V *vs.* RHE) under optimal conditions compared to pristine $BiVO_4$/$BiFeO_3$, as reported by Yuan and colleagues (−0.4 V *vs.* RHE) [19]. However, despite requiring a lower overpotential, Ag@$BiVO_4$/$BiFeO_3$ exhibits FE values nearly two times lower than those achieved for $BiVO_4$/$BiFeO_3$ in Yuan's work [19]. In comparison, catalysts from different classes, such as the metal–organic framework-based Co-PDMA-2-mbIM, demonstrate higher FE values than our system [79]. Nevertheless, despite this improvement, Co-PDMA-2-mbIM requires a substantially higher overpotential (−0.5 V *vs.* RHE), nearly 300 mV above than Ag@$BiVO_4$/$BiFeO_3$. In fact, under conventional electrochemical conditions, i.e. in the absence of light, all reported catalysts required overpotentials greater than −0.4 V *vs.* RHE to achieve significant FE values.

Importantly, LSPR-assisted electrocatalysis not only enhances selectivity by suppressing the hydrogen evolution reaction (HER), as previously discussed, but also reduces the overpotential and increases the FE. This effect is evident when comparing Ag@$BiVO_4$/$BiFeO_3$ in absence of light and LSPR. Under LSPR excitation, Ag@$BiVO_4$/$BiFeO_3$ exhibits a notable reduction in overpotential (∼300 mV) and a 2.5-fold improvement in FE compared to the absence light conditions. The difference becomes even more pronounced when comparing LSPR conditions using the Ag@$BiVO_4$/$BiFeO_3$ with $BiVO_4$/$BiFeO_3$ in the absence of light, where the overpotential is reduced by 500 mV, and an improvement of FE is observed. Therefore, LSPR excitation during N_2 and CO_2 co-electrolysis emerges as a promising strategy to fine-tune selectivity in urea electrosynthesis.

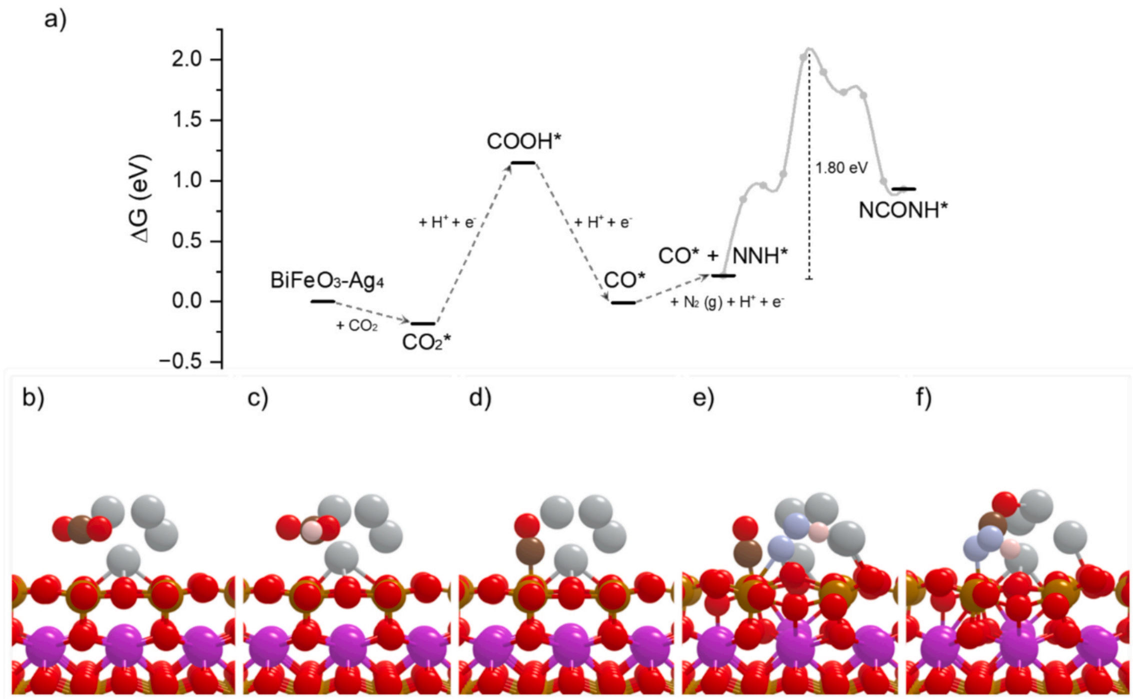

Fig. 8. Free energy profile until the coupling reaction to NCONH* over $BiFeO_3$-Ag_4 surface (a). The kinetic profile obtained with the nudged elastic band method is shown in a grey spline-connected line for the last step. Side views of $BiFeO_3$ – Ag_4 with absorbed (b) CO_2*, (c) COOH*, (d) CO, (e) CO* and NNH*, and (f) NCONH*.

Table 2
Catalysts reported for urea electrosynthesis towards the N_2 and CO_2 co-electrolysis under different conditions.

Catalyst	Potential Applied (V *vs* RHE)	Faradaic Efficiency (FE)	Reference
Ag@$BiVO_4$/$BiFeO_3$ (LSPR)	**+0.1 V**	**24.26 %**	**This work**
Ag@$BiVO_4$/$BiFeO_3$ (Dark)	**−0.2 V**	**9.52 %**	**This work**
$BiVO_4$/$BiFeO_3$	−0.4 V	17.18 %	[19]
Bi-$BiVO_4$	−0.4 V	12.55 %	[31]
Co-PDMA-2-mbIM	−0.5 V	48.97 %	[79]
Pd_1Cu_1/TiO_2-400	−0.4 V	8.92 %	[16]
$Ni_3(BO_3)_2$–150	−0.5 V	20.36 %	[18]
InOOH	−0.4 V	20.97 %	[80]
Cu-Phtalocianine	−0.6 V	12.99 %	[81]

5. Conclusions

$BiVO_4$/$BiFeO_3$ decorated with Ag NPs was synthesized by mechanochemistry and fully characterized by different techniques. As result of the milling process not only Ag NPs are produced over the oxides, but as well metallic bismuth species in a well distribution over the oxide, as confirmed by TEM images. It is possible to conclude that oxygen vacancies were formed as result of the milling process related to the changes in oxidation number of vanadium and iron species, reflecting also the changes of the charge carrier's density observed by Mott-Schottky analysis. Further XAS measurements revealed a formation of metallic silver species with a complex environment across them and oxides supports.

The electrochemical results in absence of light revealed that the reduction of $N_2 + CO_2$ occurs in a narrow potential window, in which high potentials are necessary to promote the C-N coupling resulting in lower electrochemical efficiency (FE) and urea yield rates related to the competition with HER. Upon plasmon excitation of metallic NPs, the electrochemical potential window is enlarged to lower overpotentials in the presence of $N_2 + CO_2$. Therefore, higher FE and urea yield rates are achieved at lower potentials compared to those in absence of light. It was also confirmed that the major LSPR contribution comes from Ag NPs instead of Bi NPs.

The mechanism investigation by *in situ* FTIR-RAS revealed that under LSPR conditions the enhancement of electrochemical C-N coupling is a consequence of low water availability over catalyst surface suppressing HER. Furthermore, theoretical calculations revealed that the catalyst site, $BiFeO_3$-Ag_4 plays an important role in the CO_2 energy adsorption and activation, which leads the C-N coupling in absence of light. It also confirms the complexity of catalyst structure obtained by XAS measurements.

The results derived from mechanochemistry across the complex catalyst structure can be an interesting approach for the development of new catalysts. In addition, the plasmon excitation during the electrocatalysis can be a valuable tool to tune the selectivity of activation species avoiding side reactions.

CRediT authorship contribution statement

Leandro A. Faustino: Writing – original draft, Validation, Methodology, Investigation, Formal analysis, Data curation. **Leonardo D. de Angelis:** Writing – original draft, Methodology, Investigation, Formal analysis, Data curation. **Eduardo C. de Melo:** Methodology, Investigation. **Giliandro Farias:** Writing – original draft, Methodology, Investigation, Formal analysis, Conceptualization. **Egon C. dos Santos:** Methodology, Investigation, Formal analysis, Data curation. **Caetano R. Miranda:** Writing – original draft, Supervision, Funding acquisition, Formal analysis, Conceptualization. **Ana G. Buzanich:** Methodology, Formal analysis. **Roberto M. Torresi:** Methodology, Data curation. **Paulo F.M. de Oliveira:** Writing – review & editing. **Susana I. Cordoba de Torresi:** Writing – review & editing, Validation, Supervision, Funding acquisition, Data curation, Conceptualization.

Declaration of competing interest

The authors declare that they have no known competing financial interests or personal relationships that could have appeared to influence the work reported in this paper.

Acknowledgments

The authors are thankful to Sao Paulo Research Foundation (FAPESP, 20/15230-5, 21/00675-4, 2021/08007-0, 22/04604-7, 2022/15960-9, 23/01223-5, 2024/09385-7, 24/13493-0) and CNPq (303269/2021-9 and 313430/2023-3). PFMO also acknowledge FAPESP for funding (FAPESP 2020/14955-6). The authors would also thankfully acknowledge the support of the RCGI – Research Centre for Greenhouse Gas Innovation, hosted by the University of São Paulo (USP) and sponsored by FAPESP and Shell Brasil, and the strategic importance of the support given by ANP (Brazil's National Oil, Natural Gas, and Biofuels Agency) through the R&D levy regulation. XAS experiments were performed at the BAMline at the BESSY-II storage ring (Helmholtz-Zentrum Berlin). The authors thank the Helmholtz-Zentrum Berlin für Materialien und Energie for the allocation of synchrotron radiation beamtime. The authors thank Dr. Marcelo Cecconi Portes and Prof. Ana Maria da Costa Ferreira for providing access to the EPR instrument, supported by the CEPID-Redoxoma Network (FAPESP 2013/07937-8).

Appendix A. Supplementary data

Supplementary data to this article can be found online at https://doi.org/10.1016/j.cej.2025.163072.

Data availability

Data will be made available on request.

References

[1] S. Kar, H. Sanderson, K. Roy, E. Benfenati, J. Leszczynski, Green Chemistry in the Synthesis of Pharmaceuticals, Chem. Rev. 122 (2022) 3637–3710.

[2] A.G. Inácio, C.C.B.F. Ítavo, A.M. Dias, G. dos Santos Difante, J.F. de Queiroz, L.C. S. de Oliveira, G.T. dos Santos, L.C.V. Ítavo, A new feed additive composed of urea and soluble carbohydrate coated with wax for controlled release in ruminal fluid, Sci. Rep. 12 (2022) 4487.

[3] D.R. MacFarlane, P.V. Cherepanov, J. Choi, B.H. Suryanto, R.Y. Hodgetts, J. M. Bakker, F.M.F. Vallana, A.N.J.J. Simonov, A roadmap to the ammonia economy, Joule 4 (2020) 1186–1205.

[4] R. Zhao, H. Xie, L. Chang, X. Zhang, X. Zhu, X. Tong, T. Wang, Y. Luo, P. Wei, Z. Wang, X. Sun, Recent progress in the electrochemical ammonia synthesis under ambient conditions, EnergyChem 1 (2019) 100011.

[5] N. Meng, Y. Huang, Y. Liu, Y. Yu, B. Zhang, Electrosynthesis of urea from nitrite and CO_2 over oxygen vacancy-rich ZnO porous nanosheets, Cell Rep. Phys. Sci. 2 (2021) 100378.

[6] Y. Feng, H. Yang, Y. Zhang, X. Huang, L. Li, T. Cheng, Q. Shao, Te-Doped Pd Nanocrystal for Electrochemical Urea Production by Efficiently Coupling Carbon Dioxide Reduction with Nitrite Reduction, Nano Lett. 20 (2020) 8282–8289.

[7] Y. Zhao, Y. Ding, W. Li, C. Liu, Y. Li, Z. Zhao, Y. Shan, F. Li, L. Sun, F. Li, Efficient urea electrosynthesis from carbon dioxide and nitrate via alternating Cu–W bimetallic C–N coupling sites, Nat. Commun. 14 (2023) 4491.

[8] J. Geng, S. Ji, M. Jin, C. Zhang, M. Xu, G. Wang, C. Liang, H. Zhang, Ambient Electrosynthesis of Urea with Nitrate and Carbon Dioxide over Iron-Based Dual-Sites, Angew. Chem. 62 (2023) e202210958.

[9] Y. Huang, K. Luo, W. Yang, X. Chen, M. Wang, L. Shi, L. Zhu, X. Mao, X. Ji, T. Xu, H. Zhu, X. Wang, Urea Electrosynthesis in Microbial Electrolysis Cells Using Low-cost Fe–N–C for Simultaneous N_2 and CO_2 Reduction, Ind. Eng. Chem. Res. 62 (2023) 13450–13457.

[10] Y. Huang, R. Yang, C. Wang, N. Meng, Y. Shi, Y. Yu, B. Zhang, Direct Electrosynthesis of Urea from Carbon Dioxide and Nitric Oxide, ACS Energy Lett. 7 (2022) 284–291.

[11] J.F. Brito, M.B. Costa, K. Rajeshwar, L.H. Mascaro, Ammonia production from nitrogen under simulated solar irradiation, low overpotential, and mild conditions, Electrochim. Acta 421 (2022) 140475.

[12] M.A. Mushtaq, M. Arif, G. Yasin, M. Tabish, A. Kumar, S. Ibraheem, W. Ye, S. Ajmal, J. Zhao, P. Li, J. Liu, A. Saad, X. Fang, X. Cai, S. Ji, D. Yan, Recent developments in heterogeneous electrocatalysts for ambient nitrogen reduction to ammonia: Activity, challenges, and future perspectives, Renew. Sustain. Energy Rev. 176 (2023) 113197.

[13] Z. Han, P. Wu, M. He, X. Zhuang, H. Lin, S. Han, Ammonia synthesis by electrochemical nitrogen reduction reaction - A novel energy storage way, J. Storage Mater. 55 (2022) 105684.

[14] A.R. Singh, B.A. Rohr, J.A. Schwalbe, M. Cargnello, K. Chan, T.F. Jaramillo, I. Chorkendorff, J.K. Nørskov, Electrochemical Ammonia Synthesis—The Selectivity Challenge, ACS Catal. 7 (2017) 706–709.

[15] M. Arif, M. Babar, U. Azhar, M. Sagir, M. Bilal Tahir, M. Asim Mushtaq, G. Yasin, M. Mubashir, J. Wei Roy Chong, K. Shiong Khoo, P. Loke Show, Rational design and modulation strategies of Mo-based electrocatalysts and photo/electrocatalysts towards nitrogen reduction to ammonia (NH_3), Chem. Eng. J. 451 (2023) 138320.

[16] C. Chen, X. Zhu, X. Wen, Y. Zhou, L. Zhou, H. Li, L. Tao, Q. Li, S. Du, T. Liu, D. Yan, C. Xie, Y. Zou, Y. Wang, R. Chen, J. Huo, Y. Li, J. Cheng, H. Su, X. Zhao, W. Cheng, Q. Liu, H. Lin, J. Luo, J. Chen, M. Dong, K. Cheng, C. Li, S. Wang, Coupling N_2 and CO_2 in H_2O to synthesize urea under ambient conditions, Nat. Chem. 12 (2020) 717–724.

[17] X. Wei, X. Wen, Y. Liu, C. Chen, C. Xie, D. Wang, M. Qiu, N. He, P. Zhou, W. Chen, J. Cheng, H. Lin, J. Jia, X.-Z. Fu, S. Wang, Oxygen Vacancy-Mediated Selective C–N Coupling toward Electrocatalytic Urea Synthesis, J. Am. Chem. Soc. 144 (2022) 11530–11535.

[18] M. Yuan, J. Chen, Y. Xu, R. Liu, T. Zhao, J. Zhang, Z. Ren, Z. Liu, C. Streb, H. He, C. Yang, S. Zhang, G. Zhang, Highly selective electroreduction of N_2 and CO_2 to urea over artificial frustrated Lewis pairs, Energ. Environ. Sci. 14 (2021) 6605–6615.

[19] M. Yuan, J. Chen, Y. Bai, Z. Liu, J. Zhang, T. Zhao, Q. Shi, S. Li, X. Wang, G.J.C. S. Zhang, Electrochemical C–N coupling with perovskite hybrids toward efficient urea synthesis, Chem. Sci. 12 (2021) 6048–6058.

[20] W. Wu, Y. Yang, Y. Wang, T. Lu, Q. Dong, J. Zhao, J. Niu, Q. Liu, Z. Hao, S. Song, Boosting electrosynthesis of urea from N_2 and CO_2 by defective Cu-Bi, Chem Catal. 2 (2022) 3225–3238.

[21] S. Zhang, J. Geng, Z. Zhao, M. Jin, W. Li, Y. Ye, K. Li, G. Wang, Y. Zhang, H. Yin, H. Zhang, H. Zhao, High-efficiency electrosynthesis of urea over bacterial cellulose regulated Pd–Cu bimetallic catalyst, EES Catal. 1 (2023) 45–53.

[22] M.P.S. Rodrigues, A.H.B. Dourado, A.G. Sampaio de Oliveira-Filho, A.P. de Lima Batista, M. Feil, K. Krischer, S. I. Córdoba de Torresi, Gold–Rhodium Nanoflowers for the Plasmon-Enhanced CO_2 Electroreduction Reaction upon Visible Light, ACS Catal. 13 (2023) 267–279.

[23] E. Contreras, R. Nixon, C. Litts, W. Zhang, F.M. Alcorn, P.K. Jain, Plasmon-Assisted Ammonia Electrosynthesis, J. Am. Chem. Soc. 144 (2022) 10743–10751.

[24] M.P.S. Rodrigues, A.H.B. Dourado, L.D.O. Cutolo, L.S. Parreira, T.V. Alves, T.J. A. Slater, S.J. Haigh, P.H.C. Camargo, S.I. Cordoba de Torresi, Gold–Rhodium Nanoflowers for the Plasmon-Enhanced Hydrogen Evolution Reaction under Visible Light, ACS Catal. 11 (2021) 13543–13555.

[25] C.H. Choi, K. Chung, T.-T.-H. Nguyen, D.H. Kim, Plasmon-Mediated Electrocatalysis for Sustainable Energy: From Electrochemical Conversion of Different Feedstocks to Fuel Cell Reactions, ACS Energy Lett. 3 (2018) 1415–1433.

[26] Y.-B. Sun, M. Ni, C. Chi, D.-R. Yang, X.-L. Chen, Q. Qi, J. Li, X.-H. Xia, Plasmon driven super-high HER activity of electronic structure and lattice strain engineered single atomic layer Pd@Au nanorods, Chem. Eng. J. 467 (2023) 143387.

[27] M.P.d.S. Rodrigues, V.M. Miguel, L.D. Germano, S.I. Córdoba de Torresi, Metal oxides as electrocatalysts for water splitting: On plasmon-driven enhanced activity, Electrochem. Sci. Adv. 2 (2022) e2100079.

[28] M.P.S. Rodrigues, A.H.B. Dourado, K. Krischer, S.I.C. Torresi, Gold–rhodium nanoflowers for the plasmon enhanced ethanol electrooxidation under visible light for tuning the activity and selectivity, Electrochim. Acta 420 (2022) 140439.

[29] L.A. Faustino, I.P.L. Xavier, P.F.M. Oliveira, S.I.C. Torresi, Tailoring Charge Carriers through Solid-State Mechanochemical Synthesis Bismuth Nanoparticles Directly onto $BiVO_4$ Surface, J. Braz. Chem. Soc. 35 (2024) e-20240106.

[30] J.F. Brito, P.G. Corradini, M.V.B. Zanoni, F. Marken, L.H. Mascaro, The influence of metallic Bi in $BiVO_4$ semiconductor for artificial photosynthesis, J. Alloy. Compd. 851 (2021) 156912.

[31] M. Yuan, J. Chen, Y. Bai, Z. Liu, J. Zhang, T. Zhao, Q. Wang, S. Li, H. He, G. Zhang, Unveiling Electrochemical Urea Synthesis by Co-Activation of CO_2 and N_2 with Mott–Schottky Heterostructure Catalysts, Angew. Chem. 60 (2021) 10910–10918.

[32] S.P. Singh, B. Karmakar, Oxidative control of surface plasmon resonance of bismuth nanometal in bismuth glass nanocomposites, Mater. Chem. Phys. 119 (2010) 355–358.

[33] D. Leng, T. Wang, Y. Li, Z. Huang, H. Wang, Y. Wan, X. Pei, J. Wang, Plasmonic Bismuth Nanoparticles: Thiolate Pyrolysis Synthesis, Size-Dependent LSPR Property, and Their Oxidation Behavior, Inorg. Chem. 60 (2021) 17258–17267.

[34] T. Sandu, Shape effects on localized surface plasmon resonances in metallic nanoparticles, J. Nanopart. Res. 14 (2012) 905.

[35] K.L. Kelly, E. Coronado, L.L. Zhao, G.C. Schatz, The Optical Properties of Metal Nanoparticles: The Influence of Size, Shape, and Dielectric Environment, J. Phys. Chem. B 107 (2003) 668–677.

[36] K.-C. Lee, S.-J. Lin, C.-H. Lin, C.-S. Tsai, Y.-J. Lu, Size effect of Ag nanoparticles on surface plasmon resonance, Surf. Coat. Technol. 202 (2008) 5339–5342.

[37] T. Kiba, K. Masui, Y. Inomata, A. Furumoto, M. Kawamura, Y. Abe, K.H. Kim, Control of localized surface plasmon resonance of Ag nanoparticles by changing its size and morphology, Vacuum 192 (2021) 110432.

[38] J. Wang, Z. Wang, B. Huang, Y. Ma, Y. Liu, X. Qin, X. Zhang, Y. Dai, Oxygen Vacancy Induced Band-Gap Narrowing and Enhanced Visible Light Photocatalytic Activity of ZnO, ACS Appl. Mater. Interfaces 4 (2012) 4024–4030.

[39] D. Cui, L. Wang, K. Xu, L. Ren, L. Wang, Y. Yu, Y. Du, W. Hao, Band-gap engineering of BiOCl with oxygen vacancies for efficient photooxidation properties under visible-light irradiation, J. Mater. Chem. A 6 (2018) 2193–2199.

[40] Z. Shen, X. Gao, S. Zhang, Z. Li, H. Zhao, Mechanochemistry assisted surface chemical modification on hard carbon for sodium storage: Size effect, Appl. Surf. Sci. 606 (2022) 154931.

[41] S. Singh, R.K. Sahoo, N.M. Shinde, J.M. Yun, R.S. Mane, W. Chung, K.H. Kim, Asymmetric faradaic assembly of Bi_2O_3 and MnO_2 for a high-performance hybrid electrochemical energy storage device, RSC Adv. 9 (2019) 32154–32164.

[42] G.A. Gomez-Iriarte, A. Pentón-Madrigal, L.A.S. de Oliveira, J.P. Sinnecker, XPS Study in $BiFeO_3$ Surface Modified by Argon Etching, Materials 15 (2022) 4285.

[43] K.-H. Ye, X. Yu, Z. Qiu, Y. Zhu, X. Lu, Y. Zhang, Facile synthesis of bismuth oxide/bismuth vanadate heterostructures for efficient photoelectrochemical cells, RSC Adv. 5 (2015) 34152–34156.

[44] Y. Schuhl, H. Baussart, R. Delobel, M. Le Bras, J.-M. Leroy, L. Gengembre, J. Grimblot, Study of mixed-oxide catalysts containing bismuth, vanadium and antimony. Preparation, phase composition, spectroscopic characterization and catalytic oxidation of propene, J. Chem. Soc., Faraday Trans. 1 79 (1983) 2055–2069.

[45] T.P. Debies, J.W. Rabalais, X-ray photoelectron spectra and electronic structure of Bi2X3 (X = O, S, Se, Te), Chem. Phys. 20 (1977) 277–283.

[46] P. Kumar, J. Singh, A.C. Pandey, Rational low temperature synthesis and structural investigations of ultrathin bismuth nanosheets, RSC Adv. 3 (2013) 2313–2317.

[47] H.S. Shin, H.C. Choi, Y. Jung, S.B. Kim, H.J. Song, H.J.J.C.p.l. Shin, Chemical and size effects of nanocomposites of silver and polyvinyl pyrrolidone determined by X-ray photoemission spectroscopy, J. of Chem. Phys. Lett. 383 (2004) 418–422.

[48] S. Peters, S. Peredkov, M. Neeb, W. Eberhardt, M. Al-Hada, Size-dependent XPS spectra of small supported Au-clusters, J. of, Surf. Sci. 608 (2013) 129–134.

[49] A.M. Ferraria, A.P. Carapeto, A.M.B.J.V. do Rego, X-ray photoelectron spectroscopy: Silver salts revisited, Vacuum 86 (2012) 1988–1991.

[50] M. Dubiel, J. Haug, H. Kruth, H. Hofmeister, W. Seifert, Temperature dependence of EXAFS cumulants of Ag nanoparticles in glass, J. Phys. Conf. Ser. (2009) 012123.

[51] M.L. Neidig, J. Sharma, H.-C. Yeh, J.S. Martinez, S.D. Conradson, A.P. Shreve, Ag K-edge EXAFS analysis of DNA-templated fluorescent silver nanoclusters: insight into the structural origins of emission tuning by DNA sequence variations, J. Am. Chem. Soc. 133 (2011) 11837–11839.

[52] K. Gelderman, L. Lee, S.W. Donne, Flat-Band Potential of a Semiconductor: Using the Mott–Schottky Equation, J. Chem. Educ. 84 (2007) 685.

[53] J. Lu, A. Günther, F. Schrettle, F. Mayr, S. Krohns, P. Lunkenheimer, A. Pimenov, V. D. Travkin, A.A. Mukhin, A. Loidl, On the room temperature multiferroic $BiFeO_3$: Magnetic, dielectric and thermal properties, The, Eur. Phys. J. B 75 (2010) 451–460.

[54] G. Swain, S. Sultana, J. Moma, K. Parida, Fabrication of Hierarchical Two-Dimensional MoS_2 Nanoflowers Decorated upon Cubic $CaIn_2S_4$ Microflowers: Facile Approach To Construct Novel Metal-Free p–n Heterojunction Semiconductors with Superior Charge Separation Efficiency, Inorg. Chem. 57 (2018) 10059–10071.

[55] D. Yan, H. Li, C. Chen, Y. Zou, S. Wang, Defect Engineering Strategies for Nitrogen Reduction Reactions under Ambient Conditions, Small Methods 3 (2019) 1800331.

[56] X. Yan, D. Liu, H. Cao, F. Hou, J. Liang, S.X. Dou, Nitrogen Reduction to Ammonia on Atomic-Scale Active Sites under Mild Conditions, Small Methods 3 (2019) 1800501.

[57] R.M. Lawrence, S.M. Unni, Defect induced nitrogen reduction reaction of carbon nanomaterials, Sustainable Energy Fuels 5 (2021) 3765–3790.

[58] K. Ramachandran, M. Geerthana, P. Maadeswaran, M. Navaneethan, S. Harish, R. Ramesh, α-Fe_2O_3/$AmTiO_2$ heterojunction-based photoanode with improved interfacial charge transport properties for enhanced photoelectrochemical water splitting, J. Mater. Sci. Mater. Electron. 33 (2022) 8318–8326.

[59] P.P. Sharma, J. Wu, R.M. Yadav, M. Liu, C.J. Wright, C.S. Tiwary, B.I. Yakobson, J. Lou, P.M. Ajayan, X.-D. Zhou, Nitrogen-Doped Carbon Nanotube Arrays for High-Efficiency Electrochemical Reduction of CO_2: On the Understanding of Defects, Defect Density, and Selectivity, Angew. Chem. Int. Ed. 54 (2015) 13701–13705.

[60] Y. Ren, C. Yu, X. Tan, H. Huang, Q. Wei, J. Qiu, Strategies to suppress hydrogen evolution for highly selective electrocatalytic nitrogen reduction: Challenges and perspectives, Energ. Environ. Sci. 14 (2021) 1176–1193.

[61] L.A. Faustino, L.H. Ferrer, P.F.M. de Oliveira, S.I.C. de Torresi, Beyond catalyst design for the electrochemical nitrogen reduction reaction: The crucial role of water availability in the electrolyte composition, Electrochim. Acta 519 (2025) 145842.

[62] S. Paul, S. Sarkar, A. Adalder, A. Banerjee, U.K. Ghorai, Dual metal site-mediated efficient C–N coupling toward electrochemical urea synthesis, J. Mater. Chem. A 11 (2023) 13249–13254.

[63] M. Radecka, M. Rekas, A. Trenczek-Zajac, K. Zakrzewska, Importance of the band gap energy and flat band potential for application of modified TiO_2 photoanodes in water photolysis, J. Power Sources 181 (2008) 46–55.

[64] S. Yu, A.J. Wilson, G. Kumari, X. Zhang, P.K. Jain, Opportunities and Challenges of Solar-Energy-Driven Carbon Dioxide to Fuel Conversion with Plasmonic Catalysts, ACS Energy Lett. 2 (2017) 2058–2070.

[65] M. Graf, G.B. Vonbun-Feldbauer, M.T.M. Koper, Direct and Broadband Plasmonic Charge Transfer to Enhance Water Oxidation on a Gold Electrode, ACS Nano 15 (2021) 3188–3200.

[66] S. Ganguli, A. Sekretareva, Role of an Inert Electrode Support in Plasmonic Electrocatalysis, ACS Catal. 12 (2022) 4110–4118.

[67] S. Ganguli, Z. Zhao, O. Parlak, Y. Hattori, J. Sá, A. Sekretareva, Nano-Impact Single-Entity Electrochemistry Enables Plasmon-Enhanced Electrocatalysis**, Angew. Chem. 62 (2023) e202302394.

[68] P.K. Jain, Taking the Heat Off of Plasmonic Chemistry, J. Phys. Chem. C 123 (2019) 24347–24351.

[69] A.J. Bagnall, S. Ganguli, A. Sekretareva, Hot or Not? Reassessing Mechanisms of Photocurrent Generation in Plasmon-Enhanced Electrocatalysis, Angewandte Chemie International Edition 63 (2024) e202314352.

[70] C. Zhan, B.-W. Liu, Y.-F. Huang, S. Hu, B. Ren, M. Moskovits, Z.-Q. Tian, Disentangling charge carrier from photothermal effects in plasmonic metal nanostructures, Nat. Commun. 10 (2019) 2671.

[71] X. Huang, Y. Li, S. Xie, Q. Zhao, B. Zhang, Z. Zhang, H. Sheng, J. Zhao, The Tandem Nitrate and CO_2 Reduction for Urea Electrosynthesis, Role of Surface N-Intermediates in CO2 Capture and Activation 63 (2024) e202403980.

[72] E.B. Creel, E.R. Corson, J. Eichhorn, R. Kostecki, J.J. Urban, B.D. McCloskey, Directing Selectivity of Electrochemical Carbon Dioxide Reduction Using Plasmonics, ACS Energy Lett. 4 (2019) 1098–1105.

[73] W. Ho, Reactions at Metal Surfaces Induced by Femtosecond Lasers, Tunneling Electrons, and Heating, J. Phys. Chem. 100 (1996) 13050–13060.

[74] S. Linic, P. Christopher, D.B. Ingram, Plasmonic-metal nanostructures for efficient conversion of solar to chemical energy, Nat. Mater. 10 (2011) 911–921.

[75] E.R. Corson, R. Kas, R. Kostecki, J.J. Urban, W.A. Smith, B.D. McCloskey, R. Kortlever, In Situ ATR–SEIRAS of Carbon Dioxide Reduction at a Plasmonic Silver Cathode, J. Am. Chem. Soc. 142 (2020) 11750–11762.

[76] L.D. Germano, L.D. De Angelis, A.P. De Lima Batista, A.G. Sampaio De Oliveira-Filho, S.I. Córdoba De Torresi, Plasmon enhanced oxygen evolution reaction on Au decorated $Ni(OH)_2$ nanostructures: The role of alkaline cations solvation, Applied Catalysis B: Environment and Energy 363 (2025) 124804.

[77] J.B. Khurgin, How to deal with the loss in plasmonics and metamaterials, Nat. Nanotechnol. 10 (2015) 2–6.

[78] C. Zhu, C. Wen, M. Wang, M. Zhang, Y. Geng, Z. Su, Non-metal boron atoms on a CuB12 monolayer as efficient catalytic sites for urea production, Chem. Sci. 13 (2022) 1342–1354.

[79] M. Yuan, J. Chen, H. Zhang, Q. Li, L. Zhou, C. Yang, R. Liu, Z. Liu, S. Zhang, G. Zhang, Host–guest molecular interaction promoted urea electrosynthesis over a precisely designed conductive metal–organic framework, Energ. Environ. Sci. 15 (2022) 2084–2095.

[80] M. Yuan, H. Zhang, Y. Xu, R. Liu, R. Wang, T. Zhao, J. Zhang, Z. Liu, H. He, C. Yang, S. Zhang, G. Zhang, Artificial frustrated Lewis pairs facilitating the electrochemical N_2 and CO_2 conversion to urea, Chem Catal. 2 (2022) 309–320.

[81] J. Mukherjee, S. Paul, A. Adalder, S. Kapse, R. Thapa, S. Mandal, B. Ghorai, S. Sarkar, U.K. Ghorai, Understanding the Site-Selective Electrocatalytic Co-Reduction Mechanism for Green Urea Synthesis Using Copper Phthalocyanine Nanotubes, Adv. Funct. Mater. 32 (2022) 2200882.